B3784

SPACE RIP: A PARALLEL IMAGING TECHNIQUE IN MAGNETIC RESONANCE IMAGING

By
Walid Elias Kyriakos

Submitted in partial fulfillment
Of the degree of Doctor of Science
In Physics

March 2001

UNIVERSITY OF SZEGED

SZTE Egyetemi Könyvtár
SZEGED
B 3784
13.

Foreword and acknowledgements:

In the past quarter of a century, medical imaging has revolutionized our understanding and relationship with the human body. Being able to observe the structure and inner workings of our anatomy is providing yet another source to our human quest for self discovery. The advent of novel non-invasive MRI technology has further enhanced our capabilities to observe and monitor biological processes. If "a picture is worth a thousand words", then a real-time picture must be worth thousands of pictures. This work describes the development of a technique that strives to make MRI a real-time modality.

I would like to thank all my colleagues and friends at the Brigham and Women's Hospital of Boston for their support and friendship. In particular, I'd like to thank Larry Panych, for bringing me to the Brigham and teaching me all about MRI, Robert Mulkern, for keeping me at the Brigham and being such a great source of knowledge and fun, and Ferenc Jolesz for supporting, injecting and directing my enthusiasm and my dream. It is mainly Dr. Jolesz's support that made this work possible, and his belief in it since the beginning, when it all sounded too crazy. In my eyes he remains, my favorite visionary. I would also like to thank the Physics department at the University of Szeged for considering this work for the doctoral degree.

Finally, I would like to dedicate this thesis to my mother Salwa, who has been and remains my source of love and motivation in this life, and to my father Elias, and my sisters Lina and Zeina. They all give meaning to my existence.

Walid Kyriakos.
Boston, February 19, 2001.

Contents

1 Introduction and Background 1

1.1 Motivation 1

1.2 Principles of nuclear magnetic resonance 3

1.2.1 Nuclear spin 3

1.2.2 Nuclei in a magnetic field 4

1.2.3 Resonance and coherence 6

1.2.4 Dynamics of the magnetization: The Bloch Equations 8

1.2.5 Precession of the Magnetization vector 10

1.2.6 The NMR signal and its detection 11

1.2.7 Relaxation phenomena 12

1.2.8 Free Induction Decay 14

1.2.9 Spin Echo 15

1.3 Basic principles of MRI 15

1.3.1 Magnetic field gradients and frequency encoding 15

1.3.2 Principle of phase encoding 18

1.3.3 The concept of k-space 20

1.3.4 Fourier transform imaging 20

1.3.5 Point spread function 22

1.3.6 Multi-dimensional Fourier imaging 22

1.3.7 Principle of slice selection 25
1.3.8 Contrast manipulation 26
1.3.9 Signal to Noise Ratio (SNR) 28
1.4 Imaging techniques: Pulse sequences 29
1.4.1 Spin-Echo 30
1.4.2 2-D Gradient recalled echo 31
1.4.3 RARE 32
1.4.4 Fast low-flip-angle techniques 33
1.4.5 2-D echo planar 34
1.4.6 BURST 36
1.4.7 GRASE 36
1.4.8 Keyhole Fourier imaging 37
1.5 The imaging system and parallel imaging 38
1.5.1 RF coils 38

2 The SPACE RIP method: 40
2.1 Introduction 40
2.2 Method 42
2.2.1 Encoding scheme: 42
2.3 3D extension of the SPACE RIP technique 48
2.4 Results 52
2.4.1 Simulation results: 52
2.4.2 Experimental results: 53
2.5 Discussion 59

3 Artifacts and Signal to Noise Ratio in various k-space sampling strategies 62

3.1 Introduction 62
3.2 Method 63
3.2.1 Encoding scheme: 63
3.2.2 SNR and the choice of k-space lines: 64
3.2.3 Strategy for choosing the k-space lines: 65
3.2.4 Quantification of image quality: 66
3.2.5 Computational cost: 67
3.2.6 Cardiac imaging experiments 67
3.3 Results 68
3.3.1 Regular k-space sampling: 68
3.3.2 Irregular k-space sampling: 70
3.3.3 Comparison of reconstructions using different k-space sets: . . 71
3.4 Discussion 72

4 Selective Excitation **74**
4.1 Introduction 74
4.2 Method 76
4.2.1 Encoding with sensitivity profiles of RF receiver coils: 76
4.2.2 K-space coverage: 77
4.2.3 Selective excitation: 77
4.2.4 Conditioning of the reconstruction matrix: 78
4.2.5 Pulse sequence design 79
4.2.6 Computational cost 79
4.2.7 Sensitivity profile calculation 80
4.3 Results 80
4.3.1 Simulation results: 81
4.3.2 Experimental results: 84

4.4 Discussion 85
4.5 Conclusion and Future direction: 88

List of Figures

1.1 Spinning proton model. 4
1.2 Proton orientation when field On versus field Off. 5
1.3 Time course of magnetization and T1. 6
1.4 Resonance and coherence. 7
1.5 Evolution of the transverse and longitudinal magnetizations. (a) Decay of transverse magnetization due to T2. (b) Recovery of longitudinal magnetization due to T1. 13
1.6 Free induction decay. 14
1.7 Conceptual Spin Echo model. 16
1.8 Effect of echo delay time (TE) on the magnitude of the spin echo. . . 16
1.9 Principle of frequency encoding. 17
1.10 x,y,and z gradient coils. 18
1.11 Phase memory of the magnetization due to the application of a phase encoding gradient. 19
1.12 3-D Spin-Echo imaging sequence. 23
1.13 Determinants of slice thickness. 26
1.14 Contrast reversal with variable TE. 28
1.15 Spin Echo sequence. 31
1.16 Gradient recalled echo pulse sequence. 32
1.17 The RARE sequence. 33

1.18 2-D Spin recalled echo planar sequence. 34
1.19 2-D Gradient recalled echo sequence. 35
1.20 The BURST sequence. 36
1.21 The GRASE sequence. 37

2.1 Parallel reconstruction scheme. 45
2.2 Simulation results. 54
2.3 Experimental results I 55
2.4 Experimental results II 56
2.5 Experimental results III 57
2.6 Expeimental results IV 58
2.7 Experimental results V 59

3.1 Acquisition of cardiac images using a 4 element phased array coil . . 68
3.2 Experimental cardiac imaging results using SPACE RIP 69
3.3 Experimental results using different subsampling sets 71
3.4 Reconstructions using energy distributed sets 72

4.1 SPACE RIP simulation results. 81
4.2 Hadamard shaped excitation profiles. 84
4.3 Reconstructions following Hadamard selective excitations 85
4.4 Reconstructions following smooth shaped selective excitations. 86
4.5 Schematic of a generic gradient echo pulse sequence for use with selective excitation. 87

Chapter 1

Introduction and Background

1.1 Motivation

Biologic tissue is relatively transparent to x-rays and opaque to radiation with intermediate wavelengths when proceeding from the shorter to the longer wavelengths of the electromagnetic spectrum. This is true for ultraviolet, visible and to some extent infrared light and microwaves. However, there is a window in tissue absorption through which radiowaves can be used to probe deep inside the human body. This window is used in MRI.

Nuclear Magnetic Resonance (NMR) has been developed since 1973 as an imaging method to map the spatial distribution of substances within an object. It has since then become one of the most important state-of-the art techniques in use for diagnostic medicine. Among the many human body imaging modalities available currently, MRI is non-invasive and provides excellent soft-tissue contrast without using harmful ionizing radiation. Clinical MRI utilizes the NMR signals generated by the ^{1}H nuclei whose natural abundance in the human body (in water and fat) and high NMR sensitivity make them ideal candidates for use in diagnostic imaging.

Of all the commonly available diagnostic imaging modalities such as ultra-sound,

fluoroscopy, and computed tomography, magnetic resonance ranks among the slowest. The long scan times of MRI are justified only by the high-quality and diagnostic efficacy of the images, but they present a number of limitations to the applications where physiologic motion or dynamic change occurs within the imaged area. Many physiological processes (Respiration, pulsatile flow, etc.) take place rapidly compared to the total time needed to acquire one image resulting in the appearance of motion artifacts that take the form of blurring or ghost effects. The same happens when trying to monitor an induced change like the insertion of a catheter or the passage of a contrast agent.

Important new applications in Functional MRI, Interventional MRI as well as any application of dynamic MRI would be greatly served by more rapid imaging techniques. While a number of techniques have been designed to increase imaging speed, a high price is usually paid in terms of spatial resolution and Signal-to-Noise Ratio.

This thesis reports in chapter 2, the development implementation and optimization of a speed enhancement technique named SPACE-RIP (Sensitivity Profiles from an Array of Coils for Encoding and Reconstruction In Parallel). It is based on the use of three-dimensional sensitivity profile functions from multiple receiver coil arrays, as spatial encoding functions. This is done in order to accelerate the imaging speed by a factor equal to the number of coils in the array. In addition, this thesis studies in chapter 3, the interrelationship between the Signal-to-Noise Ratio (SNR) and the image resolution achieved by SPACE RIP, as a function of the k-space sampling pattern. In chapter 4, we show how the use of 2D selective excitation in conjunction with parallel imaging can allow for a preservation of image resolution and SNR in accelerated images.

1.2 Principles of nuclear magnetic resonance

1.2.1 Nuclear spin

Certain atomic nuclei that have an odd number of protons or neutrons possess a characteristic known as "spin". This characteristic was suggested by Wolfgang Pauli in 1924 [1] as a way to describe the complex structure of atomic spectra. Accordingly, protons in the nuclei spin at high speed generating an angular momentum, $\vec{I}$, due to their mass and a magnetic moment, $\vec{\mu}$, due to their charge. Although electrically neutral, neutrons are also thought to generate a magnetic moment of about two thirds that of the protons due to the non-uniform distribution of electrical charge within their volume. When the numbers of protons and neutrons are even, their magnetic moments are paired and cancel out leaving the atom with zero net spin angular momentum. However, when an odd number of protons, neutrons or both exists, the atom exhibits a net spin and hence a net magnetic moment.

The existence of the spin property is a necessary condition for the occurrence of the Nuclear Magnetic Resonance (NMR) phenomenon [2]. Some nuclei that possess spin are ^{1}H, ^{13}C, ^{19}F, and ^{23}Na. ^{1}H is of most interest in imaging because of its natural abundance especially in tissue. It can also be easily modeled due to the fact that it only possesses one proton. Figure 1.1 shows the conceptualization of a spinning proton of angular momentum, $\vec{I}$, generating a magnetic moment, $\vec{\mu}$. The magnetic field produced in the neighborhood of the proton is analogous to that of a microscopic bar magnet having a north (N) and a south (S) poles. The angular momentum and the magnetic moment are related by a constant, γ, called the gyromagnetic ratio such that

$$\vec{\mu} = \gamma \vec{I}. \tag{1.1}$$

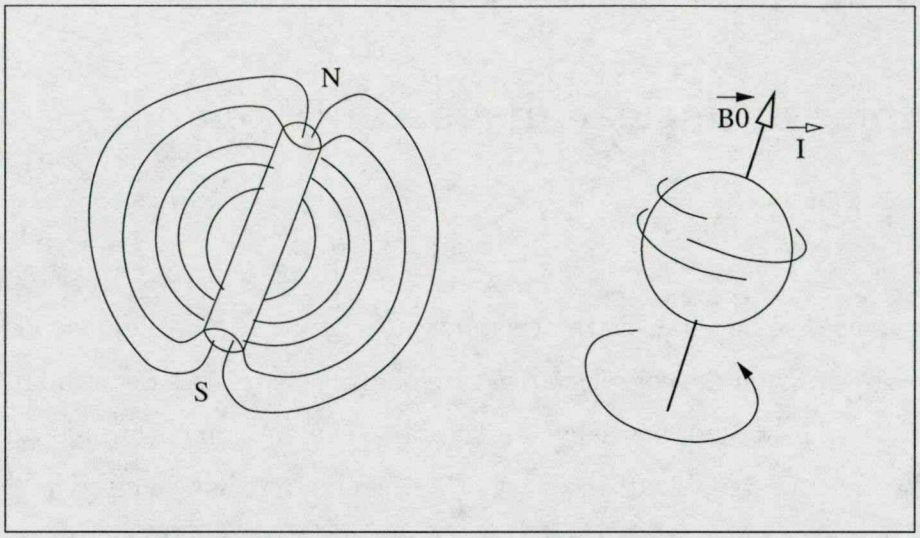

Figure 1.1: Spinning proton model.

1.2.2 Nuclei in a magnetic field

In the presence of an external magnetic field B_0, spinning protons that are initially randomly oriented magnetic dipoles, line up with the magnetic field. Their energy states are determined by quantum mechanics and can assume 2I+1 values [3] where I can be an integer in some cases (eg: ^{2}H, ^{14}N) or a half integer in others (eg: ^{1}H, ^{13}C, ^{31}P, ^{23}Na). In the case of ^{1}H, the value of I is $\frac{1}{2}$, therefore a proton can only have two energy states. By convention, we consider the north pointing direction as having the lower energy level, and therefore being more stable than the south pointing direction. Figure 1.2 shows the difference in proton direction when the magnetic field is On or Off. The difference in energy, ΔE, between the two states is a function of the applied magnetic field [4] and can be written as

$$\Delta\ E = 2\mu\ B_0, \tag{1.2}$$

where μ is the magnetic moment and B_0 is the externally applied magnetic field.

Due to the greater stability of the north pointing direction, protons tend to as-

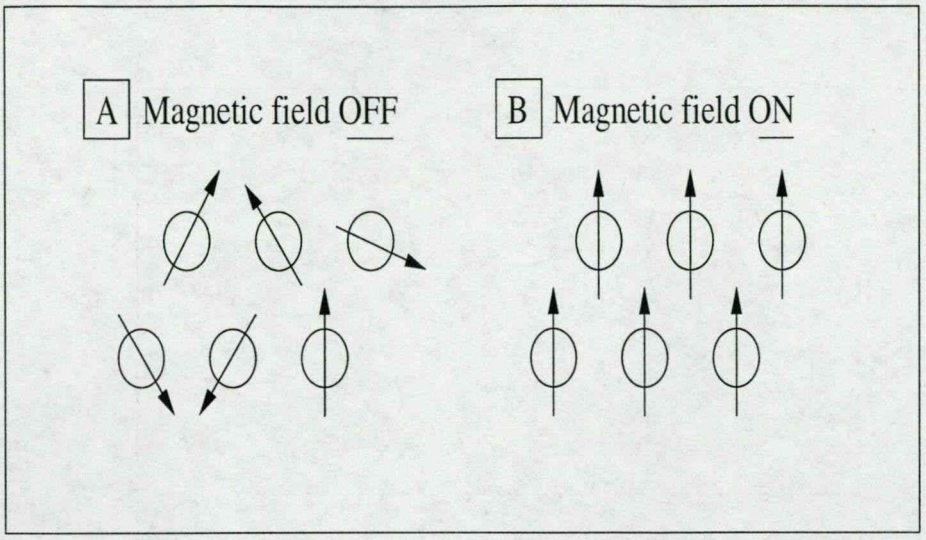

Figure 1.2: Proton orientation when field On versus field Off.

sume it after the application of the external magnetic field. At 0°K, all protons would assume the north pointing direction. At higher temperatures, however, protons undergo thermal flipping, and jump randomly from the low to high energy level and vice versa. This behaviour can be detected as noise by an antenna of a radio receiver if it were placed near the magnetized object. After an equilibrium is established, however, there is a net magnetization of the sample. This equilibrium magnetization, M_0, is given by Curie's law [3]:

$$M_0 = \frac{\gamma^2 \hbar^2 \ I(I+1)}{3kT} \ H_0 \tag{1.3}$$

where γ is the gyromagnetic ratio, $\hbar$ is Planck's constant, k is Boltzmann's constant, T is temperature in ^oK, and H_0 is proportional to the static magnetic field B_0. Figure 1.3 shows the evolution of the magnetization as protons are subjected to an external magnetic field. After the application of that field, magnetization occurs rapidly at first but its rate of increase becomes smaller as it approaches the maximum equilibrium value M_0. This increase takes the form of an exponential and can be

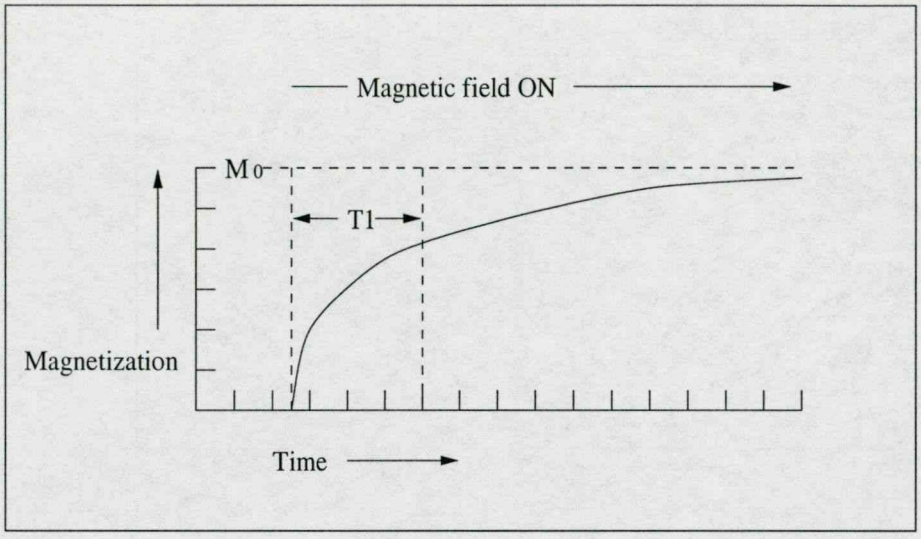

Figure 1.3: Time course of magnetization and T1.

written as

$$M(t) = M_0(1 - e^{-\frac{t}{T1}}), \tag{1.4}$$

where T1 is a time constant characteristic of the nuclear environment [5].

1.2.3 Resonance and coherence

If the magnetized object is subjected to a short burst of radio frequency (RF) energy at a specific frequency, a signal is detected by the antenna indicating the fact that the nuclei are precessing in phase and emitting a coherent signal. This phenomenon is called resonance [6] and can only occur at a frequency determined by the external magnetic field. Resonance only occurs when the energy of the RF photons matches the energy difference between allowed orientations of the nuclei. Thus, from this energy difference as expressed in Eq. 1.2:

$$\Delta E = \hbar\omega = 2\mu B_0 = 2\gamma\hbar IB_0, \tag{1.5}$$

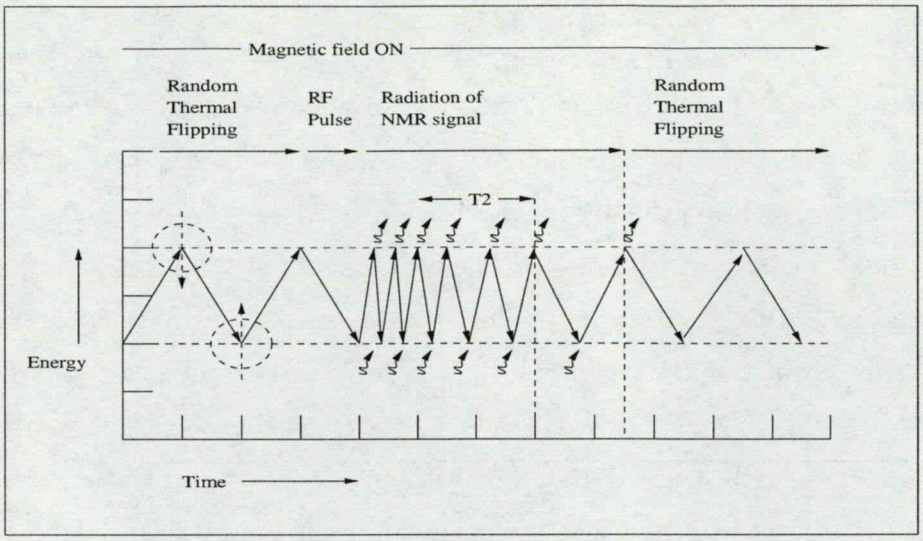

Figure 1.4: Resonance and coherence.

and, if I equals $\frac{1}{2}$, then $\omega = \gamma\ B_0$, where ω is the angular frequency in radians per second and B_0 is the static magnetic field.

For a short period after the RF transmitter is turned off, we can continue to detect an RF signal by the antenna. Assuming a perfectly homogeneous B_0 field, the decay of this signal is characterized by another time constant, T2, describing the loss of coherence [7]. The principles of resonance and coherence are described in Fig. 1.4 where random thermal flipping is shown followed by resonance occurring with the application of the RF pulse. After removing the RF excitation, the nuclei continue to radiate until coherence is eventually lost. The detection of the NMR signal depends on the existence of coherence.

1.2.4 Dynamics of the magnetization: The Bloch Equations

The discussion of the previous section is based on the principles of quantum and statistical mechanics. For almost all imaging applications, however, the behaviour of the nuclear magnetization can be adequately described by classical equations of motion of a vector, $\vec{M}$, representing the net magnetization. In the following discussion we refer to the components of $\vec{M}$ which are: (1) The component, M_z, aligned with the B_0 field and referred to as the longitudinal magnetization; and (2) a component, $\vec{m}$, referred to as the transverse magnetization which is usually expressed as a complex quantity equal to $M_x + iM_y$.

In 1947, Felix Bloch described the dynamic behaviour of the magnetization vector [8]. This result can be reached by either the classical or the quantum mechanical descriptions. In the classical description, a system has a net angular momentum given by $\vec{J}$, and a net magnetic moment defined as $\vec{M} = \gamma\vec{J}$. In a magnetic field $\vec{B}$, and in the absence of frictional losses, the magnetic moment, $\vec{M}$, experiences a torque $\vec{T}$ [4] given by

$$\vec{T} = \vec{M} \wedge \vec{B}. \tag{1.6}$$

This torque is equal to the rate of change of its angular momentum, $\vec{J}$ [4].

$$\frac{d\vec{J}}{dt} = \vec{T}. \tag{1.7}$$

Using

$$\vec{M} = \gamma\vec{J}, \tag{1.8}$$

we get

$$\frac{d\vec{M}}{dt} = \gamma\frac{d\vec{J}}{dt} = \gamma\vec{T}. \tag{1.9}$$

Therefore,

$$\frac{d\vec{M}}{dt} = \gamma\vec{M} \wedge \vec{B}. \tag{1.10}$$

This description of $\vec{M}$ is in a fixed coordinate system. To describe $\vec{M}$ in the relative frame rotating at the angular velocity, ω, of the spins, we use the general law of relative motion [1]. This law stipulates that given two coordinate systems (S1) and (S2) where the rotation vector of (S2) with respect to (S1) is a known function of time, $\vec{\omega}(t)$,the following relation holds:

$$(\frac{d\vec{M}(t)}{dt})_{s1} = (\frac{d\vec{M}(t)}{dt})_{s2} + (\vec{\omega}(t) \wedge \vec{M}(t))_{s2}, \tag{1.11}$$

where $(d\vec{M}/dt)_{S1}$ is the time derivative of $\vec{M}(t)$ in S1 and $(d\vec{M}/dt)_{S2}$ is the time derivative of $\vec{M}(t)$ in S2. If $\vec{x_1}, \vec{y_1}, \vec{z_1}$ are the axes of (S1), and $\vec{x_2}, \vec{y_2}, \vec{z_2}$ are the axes of (S2), we pick $\vec{z_2}$ to coincide with $\vec{z_1}$. If the angular velocity of (S2) with respect to (S1) is ω in the (x,y) plane, then the rotation vector of (S2) with respect to (S1) is $\vec{\omega}(t) = \omega\vec{z}$. Hence, we can write Eq 1.10 in the rotating frame as

$$(\frac{d\vec{M}}{dt})_r = \gamma\vec{M} \wedge \vec{B} + (\vec{\omega} \wedge \vec{M}). \tag{1.12}$$

Therefore,

$$(\frac{d\vec{M}}{dt})_r = \gamma\vec{M} \wedge \vec{B} - (\vec{M} \wedge \vec{\omega}) = [\gamma\vec{M} \wedge (\vec{B} - \frac{\vec{\omega}}{\gamma})], \tag{1.13}$$

where $(\vec{B} - \vec{\omega}/\gamma)$ can be considered as the effective field, $\vec{B_{eff}}$, in the rotating frame.

Equation 1.13 describes the magnetization vector of a free spin in the rotating frame in the absence of losses. Adding those losses in the form of $f(\vec{M})$ would yield

$$(\frac{d\vec{M}}{dt})_r = \gamma\vec{M} \wedge \vec{B}_{eff} + f(\vec{M}). \tag{1.14}$$

In the absence of the RF field, and considering the $\vec{B}$ field to be in the z-direction, we can write the equations in the rotating frame as

$$\frac{dM_z}{dt} = \frac{M_0 - M_z}{T1}, \tag{1.15}$$

$$\frac{dm}{dt} = -i\gamma\, mB_{eff} - \frac{m}{T2}, \tag{1.16}$$

where T1 and T2 are the time constants of relaxation processes described earlier. M_0 is the sample magnetization at equilibrium. M_z and m are the components of the nuclear magnetization vector in the z-direction and in the transverse plane respectively. B_{eff} is the effective field in the z-direction and γ is the gyromagnetic ratio. Solving the two equations to obtain the expressions for the transverse and longitudinal components of the magnetization we get that

$$m(t) = m(0)e^{(-(i\gamma \int B_{eff}dt) - \frac{t}{T2})}, \quad \text{and} \tag{1.17}$$

$$M_z(t) = M_z(0)e^{-(\frac{t}{T1})} + M_0(1 - e^{(-\frac{t}{T1})}). \tag{1.18}$$

The signal collected at the RF coil is generated by the time variation of the transverse magnetization m(t).

1.2.5 Precession of the Magnetization vector

We consider two reference frames: (S1) fixed to the lab and having $(\vec{x_1}, \vec{y_1}, \vec{z})$ as axes, and (S2) as the rotating frame having $(\vec{x_2}, \vec{y_2}, \vec{z})$ as axes. We apply an RF field of frequency, ω, in the $\vec{x_2}$ direction to a sample where the applied magnetic field is $B_0\vec{z} = \frac{\omega}{\gamma}\vec{z}$. In the fixed frame (S1), the magnetization vector precesses around $\vec{z}$ at a frequency ω as it angles away from it at an angular velocity η such that

$$\frac{\omega}{\eta} = \frac{B_0}{B1}, \tag{1.19}$$

where B_0 is the magnitude of the static magnetic field and $B1$ is the magnitude of the RF field. Since B_0 is much greater than $B1$, ω is much greater than η.

In the rotating frame B_{eff} is comparable to $B1$ and, at resonance, the z-component of B_{eff} is equal to zero. Therefore, in a frame rotating at the resonant frequency of the spins, the magnetization vector does not precess about $\vec{z}$. For an RF field of the

same frequency and in phase with the rotating frame axis $\vec{x_2}$, and of strength B1, the magnetization vector precesses about x_2 with a frequency η. The angle, θ, of the tipping away from $\vec{z}$ due to an RF field depends on the time, τ, during which the RF field is applied, such that $\theta = \gamma\ B1\ \tau$. In the off-resonance case and in the absence of the RF field, the magnetization rotates around the z-axis at a frequency proportional to the off-resonance field.

1.2.6 The NMR signal and its detection

After tipping the magnetization vector by a certain angle α, it will have a component in the transverse plane rotating around $\vec{z}$ at the precession frequency ω_0. If an RF coil is placed perpendicularly to the transverse plane, the sinusoidal variation of the transverse magnetization will induce a current in the coil. This current will have the same frequency, ω_0, and constitutes the acquired NMR signal.

We can only record the signal from a sum of the magnetization vectors throughout the volume. This signal can be written as a time varying sinusoidal quantity,

$$s_f(t) = a(t)cos(\omega_0\ t + \phi\ (t)). \tag{1.20}$$

We wish to transfer to the rotating frame obtaining the complex quantity

$$s(t) = a(t)exp(-i\phi\ (t)). \tag{1.21}$$

This is done in the following steps.

1) We mix $s_f(t)$ and $cos(\omega_0\ t)$ to obtain

$$\begin{aligned} s(t)cos(\omega_0\ t) &= a(t)cos(\omega_0\ t + \phi(t))cos(\omega_0\ t) \\ &= \frac{a(t)}{2}[cos(2\omega_0\ t + \phi(t)) + cos(\phi(t))]. \end{aligned} \tag{1.22}$$

The Fourier Transform of this signal is given by two pairs of Dirac delta functions at $\pm[2\omega_0 + \phi(\omega)]$ and at $\pm[\phi(\omega)]$. By applying a low-pass filter that includes frequencies

up to $\phi(\omega)$, we get a signal $s_r(t)$ such that

$$s_r(t) = \frac{a(t)}{2} cos(\phi(t)). \tag{1.23}$$

2) We mix $s_f(t)$ with $sin(\omega_0)\ t$ to obtain

$$\begin{aligned} s(t)sin(\omega_0\ t) &= a(t)cos(\omega_0\ t + \phi(t))sin(\omega_0\ t) \\ &= \frac{a(t)}{2}[sin(2\omega_0\ t + \phi(t)) + sin(\phi(t))]. \end{aligned} \tag{1.24}$$

The Fourier Transform of this signal is given by two pairs of Dirac Delta functions at $\pm[2\omega_0 + \phi(\omega)]$ and at $\pm[\phi(\omega)]$. We apply a low-pass filter to this signal to get a signal $s_i(t)$ such that

$$s_i(t) = \frac{a(t)}{2} sin(\phi(t)). \tag{1.25}$$

3) We combine the signals obtained from the first two steps to get

$$s(t) = 2[s_r(t) - is_i(t)] = a(t)[cos(\phi(t)) - isin(\phi t)] = a(t)e^{-i\phi(t)}, \tag{1.26}$$

which is the signal used to make the image.

For the rest of this thesis, unless stated otherwise, we consider the magnetization vector to be in the rotating frame.

1.2.7 Relaxation phenomena

Following a 90 degree RF pulse, the magnetization vector, $\vec{M}$, lies in the transverse plane and its longitudinal component is zero. When the RF field is off, nuclei are only subjected to the external magnetic field B_0, and the longitudinal magnetization recovers to M_0 at an exponential rate with time constant T1. T1 depends on the magnetic field strength, on temperature and on the sample viscosity [9].

In the presence of a perfectly uniform applied field, coherence is lost due to microscopic field inhomogeneities due to dynamic molecular interactions in the sample.

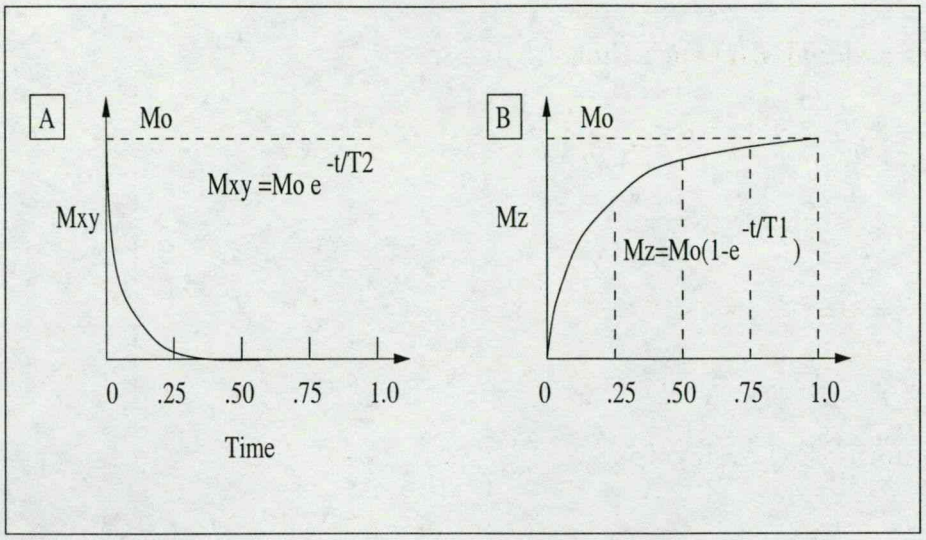

Figure 1.5: Evolution of the transverse and longitudinal magnetizations. (a) Decay of transverse magnetization due to T2. (b) Recovery of longitudinal magnetization due to T1.

This results in the decay of the transverse magnetization M_{xy} at an exponential rate with time constant T2 [7]. The relationship between loss of transverse and recovery of longitudinal magnetizations is shown in Fig. 1.5.

In the practical situation however, the transverse magnetization is lost at an even faster rate than T2 because of static field inhomogeneities due to intrinsic field inhomogeneity, chemical shift, and magnetic susceptibility differences. This rate is an exponential with time constant T2* [7]. It can be shown that loss of coherence due to inhomogeneities in the applied field can be reversed by the application of a 180 ^{o} RF pulse as will be discussed in section 2.1.9. Loss of coherence due to T2 cannot be reversed.

SZTE Egyetemi Könyvtár SZEGED

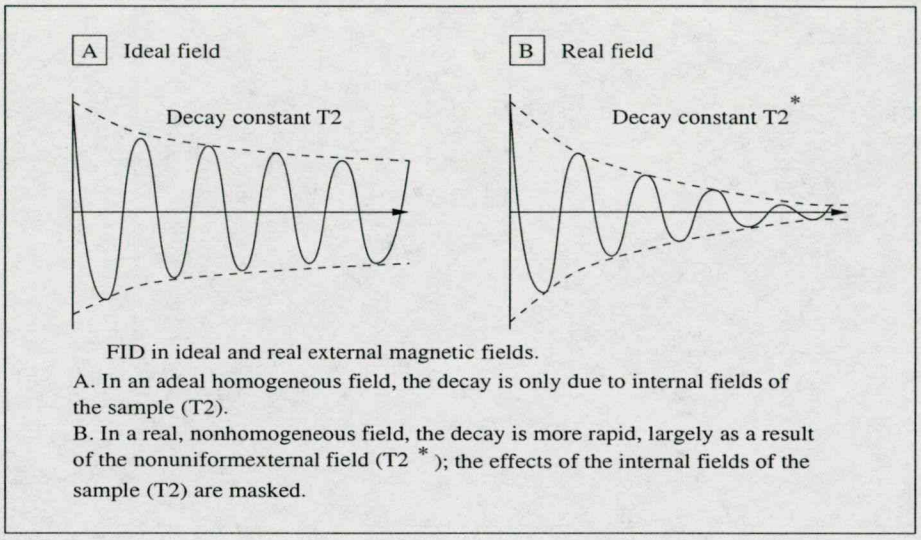

FID in ideal and real external magnetic fields.
A. In an adeal homogeneous field, the decay is only due to internal fields of the sample (T2).
B. In a real, nonhomogeneous field, the decay is more rapid, largely as a result of the nonuniformexternal field (T2 *); the effects of the internal fields of the sample (T2) are masked.

Figure 1.6: Free induction decay.

1.2.8 Free Induction Decay

At the end of a 90 degree RF pulse, the magnetization is subjected only to the static external magnetic field about which it precesses. If a coil is placed perpendicularly to the transverse plane, an AC voltage is induced in it due to the precession of the magnetization vector. Loss of coherence due to T2 and T2* causes a decay of this signal. This voltage can be written as

$$V = M_0 e^{(i\omega\ t - \frac{t}{T2})} e^{(-\frac{t}{T2*})} \tag{1.27}$$

This is a complex quantity that decays to zero. The induced voltage is called the Free Induction Decay (FID) [4]. It is shown in Fig. 1.6 for both the ideal field with T2 decay only, and the real field where T2* decay dominates.

1.2.9 Spin Echo

Following a 90 ^{o} pulse in a perfectly homogeneous field, the detected signal decays with a time constant T2. As discussed previously, the transverse magnetization decays at a much faster rate with another time constant T2* due to the spatial inhomogeneity of the magnetic field. This is due to the loss of coherence between the spins as they experience slightly different field strengths. A 180 degree RF pulse applied at some time following the 90 degree pulse can be shown to reestablish the phase coherence lost due to external field inhomogeneity. The signal that arises due to the re-establishment of coherence following the 180^o pulse is known as the Spin Echo [1].

Figure 1.7 shows a conceptual model of the behavior of the spins during a Spin Echo experiment where, in Fig¿ 1.7(a), the magnetization vector is represented by a single vector precessing in the xy plane following the establishment of coherence. In Fig. 1.7(b), there is a decay of the net transverse magnetization due to dephasing of the local magnetization vectors. Nuclei shown on the leading edge are in a slightly higher field than those shown on the lagging edge. In Fig. 1.7(c), after the application of a 180^o RF pulse, the nuclei precessing at a faster rate are now on the lagging edge while those precessing at a slower rate are on the leading edge. This results in a reversal of the dephasing of the magnetization. In Fig. 1.7(d) shows the spin-echo is formed as a result of reestablishment of coherence between all the local magnetization vectors.

1.3 Basic principles of MRI

1.3.1 Magnetic field gradients and frequency encoding

Nuclear Magnetic resonance imaging is based on the fact that the resonant frequency,f, of the local magnetization vectors is a function of the externally applied B field, where

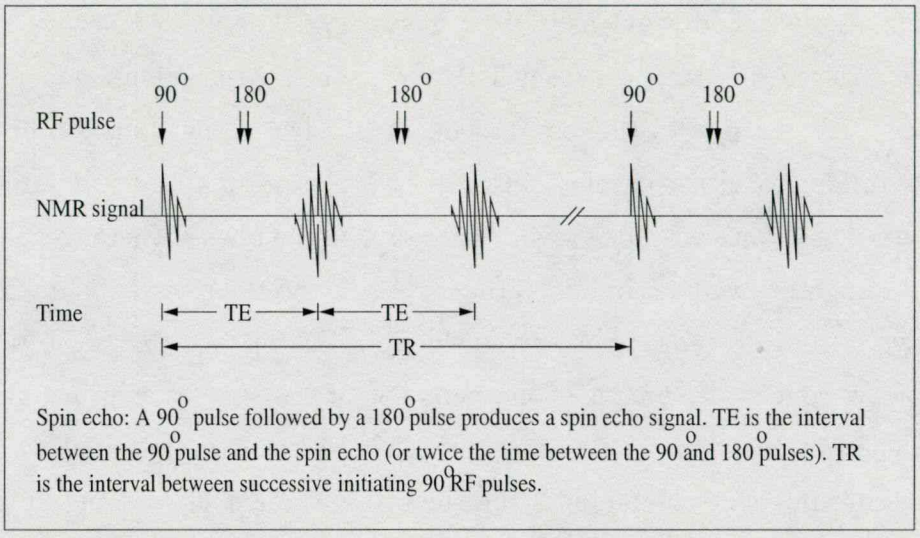

Spin echo: A 90^{o} pulse followed by a 180^{o} pulse produces a spin echo signal. TE is the interval between the 90^{o} pulse and the spin echo (or twice the time between the 90^{o} and 180^{o} pulses). TR is the interval between successive initiating 90^{o} RF pulses.

Figure 1.7: Conceptual Spin Echo model.

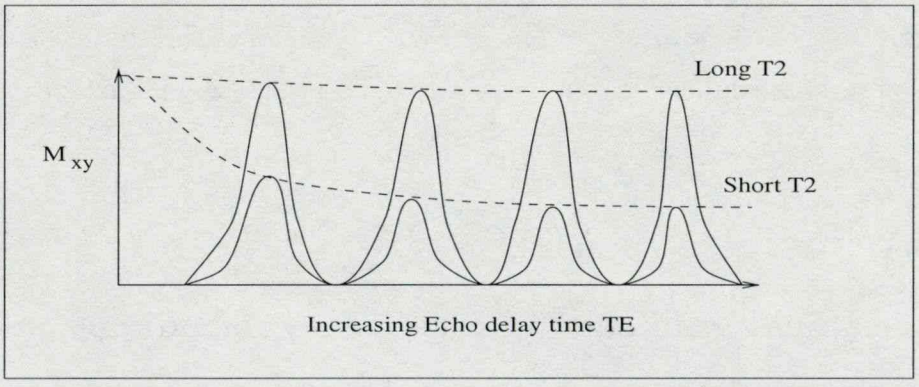

Figure 1.8: Effect of echo delay time (TE) on the magnitude of the spin echo.

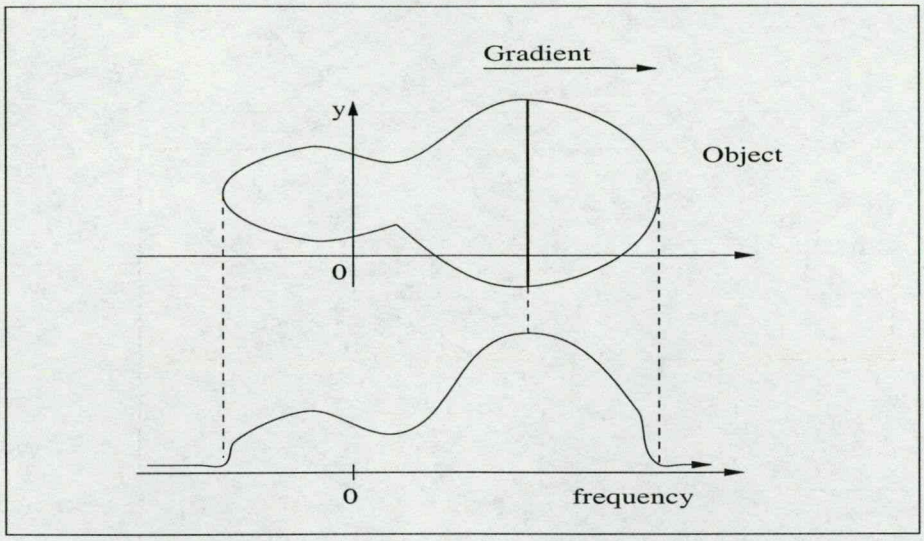

Figure 1.9: Principle of frequency encoding.

$f = \gamma Bo/2\pi$. An important feature of NMR imaging systems is the gradient coil set which makes spatial encoding possible [3]. A gradient coil generates a magnetic field which adds a small offset to the main field. This offset field changes linearly with position along a certain direction and can be switched on and off relatively rapidly. The direct result of this is that the resonant frequency of a sample placed in that gradient can be made to vary linearly with position.

When an RF field is applied to a sample placed in a field gradient, the acquired signal contains all the frequencies radiated by the sample. Since there is a linear mapping between position and resonant frequencies, the spectral density of the acquired signal represents a spatial density distribution as demonstrated by Fig. 1.9. This principle is called frequency encoding [10]. When a Fourier Transform is performed on the acquired signal, it gives the projection of the 3-dimensional space onto the coordinate axis in the gradient direction [10].

Linear gradients are used to encode spatial position in all 3 directions. The z

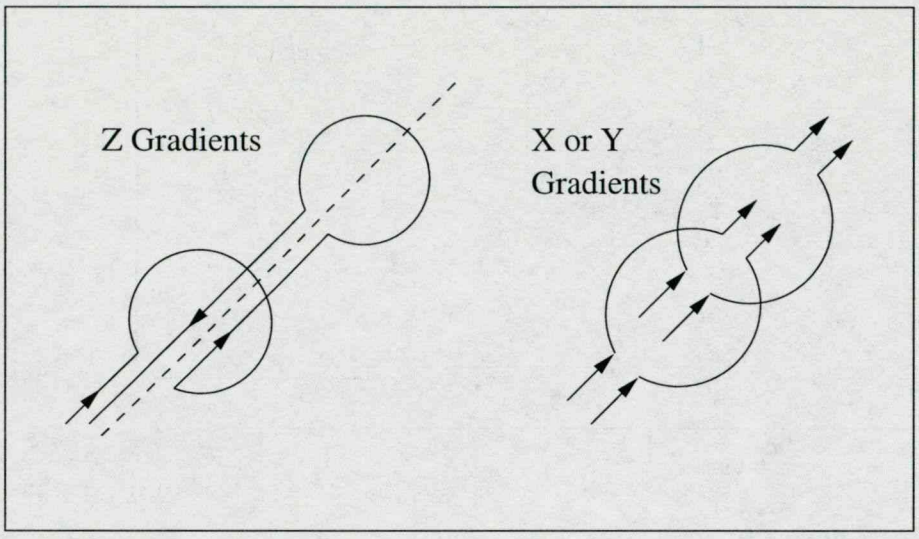

Figure 1.10: x,y,and z gradient coils.

gradient consists of coils with counter circulating current. The x and y gradients consist of separate arcs with counter circulating currents. These gradient coils are shown in Fig. 1.10. The overall magnetic field $\vec{B_G}$ created by the gradient coils is in the same direction as the main field, $\vec{B_0}$, and can be written as:

$$\vec{B_G} = (G_x x + G_y y + G_z z)\vec{z} \tag{1.28}$$

where x, y, and z are the spatial coordinates and G_x, G_y, and G_z are proportional to the current in the coils.

1.3.2 Principle of phase encoding

Frequency encoding is based on the fact that resonant frequency depends on the external field and that it is varied with position. This is possible to achieve in one

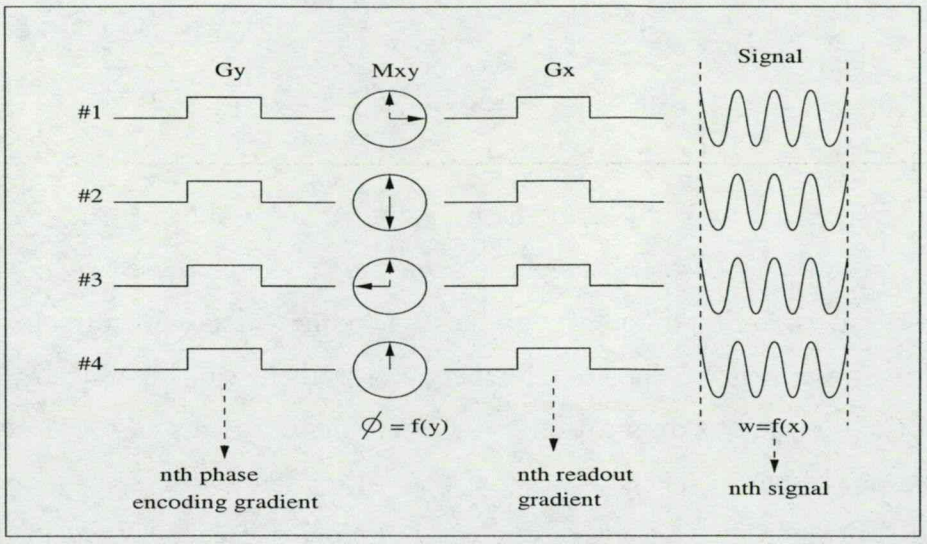

Figure 1.11: Phase memory of the magnetization due to the application of a phase encoding gradient.

dimension where we superimpose a linear field gradient on the static field, $\vec{B_0}$, in order to uniquely map resonant frequency to spatial location. It is, however, not possible to achieve a unique $\vec{B}$ field mapping of 2-D and 3-D space because the continuity condition that must be satisfied. Therefore, in order to encode spatial position in two or three dimensions the principle of phase encoding must be applied [4].

Let us consider the case of two-dimensional encoding with directions being x and y, and assuming that the x direction is frequency encoded. After the application of the RF field, the spins flip by a certain angle and start precessing around the z-axis. If we apply a gradient, Gy, in the y direction for a period Δty, they will precess at different frequencies in the y-direction and therefore accumulate a different phase, ϕy, that is a linear function of y (Fig. 1.11). At the end of Δty, the phase gradient Gy is turned off. Now all the spins will resonate at the same frequency, however their phases will depend on their position along y. They are said to have phase memory. If now we turn on the x-gradient and acquire the signal, we will have a frequency

encoded signal of the x direction containing a phase encoding of the y direction as shown in Fig. 1.11.

By varying the magnitude of the y-gradient by ΔGy for multiple frequency encoded acquisitions, we get a variation of the phase angle $\Delta\phi$y. Therefore, to encode n pixels in the y direction, we need n different y-gradient encodings. The same principle can be applied for three-dimensional encoding where a z gradient can be applied to encode the z direction during the application of the y gradient. In this case, if m is the number of volume elements (voxels) needed in the y direction and n is the number of voxels needed in the z direction, then the total number of frequency encoded acquisitions (which is usually also equal to the number of excitations) that are needed to cover the whole volume is m$\times$n.

1.3.3 The concept of k-space

In MRI, the concept of "k-space" is often used to aid in the conceptualization and analysis of imaging techniques [11]. It is an abstract space representing the frequency space of the object being imaged. In Fourier Transform MRI, when acquiring data, we are sampling k-space and the order of that sampling by the image sequence is referred to as the 'k-space trajectory'. Most imaging sequences are generally distinguished by their k-space trajectories. Since k-space represents spatial frequency information, it can be sampled along one, two or three dimensions and an image is made by taking the Fourier-Transform of the acquired data-set.

1.3.4 Fourier transform imaging

Before discussing imaging sequences in detail, a simple 1-D description of Fourier transform imaging [10] will help to demonstrate the basic principles. Here we make use of the solutions to the Bloch equations for the time varying transverse magnetization

vector (Eq. 1.17) in the absence of the RF field.

After the application of an RF pulse that tips the magnetization into the transverse plane, the gradient field is turned on briefly. From Eq. 1.17, we can write the transverse magnetization at a location x and at time t as

$$m(x,t) = m(x,0)e^{[-(i\gamma \int Bdt) - \frac{t}{T2}]}, \tag{1.29}$$

where B is the effective field strength in the rotating frame. In the case where T2 decay is insignificant, Eq. 1.29 becomes

$$m(x,t) = m(x,0)e^{-i\gamma \int B(x,t)dt}. \tag{1.30}$$

The actual recorded signal being the contribution of all spins throughout space (only x in this simple case), it can be written as

$$s(t) = \int m(x,t) = \int m(x,0)e^{-i\gamma \int B(x,t)dt}. \tag{1.31}$$

Note that s(t) is extracted from the signal given in Eq. 1.20 after it is filtered and transformed into the phasor given by Equation 1.21. We assume that only the gradient field is significant so that B(x,t)=$G_x x$. Therefore we can write

$$s(t) = \int s(x)e^{-i\gamma \int G_x dt\ x}dx, \tag{1.32}$$

where s(x) is proportional to m(x,0).

Applying the change of variables such that $k = \gamma \int G_x dt$, we can write Eq. 1.32 in the following way:

$$s(k) = \int s(x)e^{-ikx}dx. \tag{1.33}$$

By collecting the signal in time, we are sampling the k-space of the image represented by s(x). The Fourier Transform of s(k) will give us s(x).

1.3.5 Point spread function

Generally, the acquired signal, s(t), contains a time-dependent term such as the T2 relaxation term, $e^{-\frac{t}{T2}}$, or more generally f(t). Thus, s(t) cannot generally be written as a Fourier Transform of s(x). In general, s(t) is written as

$$s(t) = \int s(x) f(t) e^{-i\gamma\, G_x t x} dx. \tag{1.34}$$

Making the change of variables such that $k = \gamma\, G_x t$ so that $t = \frac{k}{\gamma\, G_x}$ we get

$$s(k) = f(k) \int s(x) e^{-ikx} dx. \tag{1.35}$$

The inverse Fourier transform of Eq. 1.35 gives

$$S(x) = \int f(k) \int s(x) e^{-ikx} dx\; e^{ikx'} dk \tag{1.36}$$

$$= \int s(x) \int f(k) e^{ik(x'-x)} dk\; dx \tag{1.37}$$

$$= \int s(x)\; f(x' - x)\; dx = s(x) *\; f(x). \tag{1.38}$$

The net result of this convolution is a distortion of the image with a "point spread function" [10], f(x),where f(x) is the inverse Fourier transform of f(t).

1.3.6 Multi-dimensional Fourier imaging

Multi-dimensional imaging requires many excitations and acquisitions. The time organization of the RF excitations, the gradient switching and the signal aquisition is called a pulse sequence. Pulse sequences will be treated into more detail in Section 2.2.10, however, for the purpose of explaining multi-dimensional imaging, we will describe the behavior of the magnetization during the 3-D spin-echo imaging sequence [12] shown in Fig. 1.12. This sequence consists of the application of a 90 degree RF pulse to the sample to put its magnetization vector into the transverse

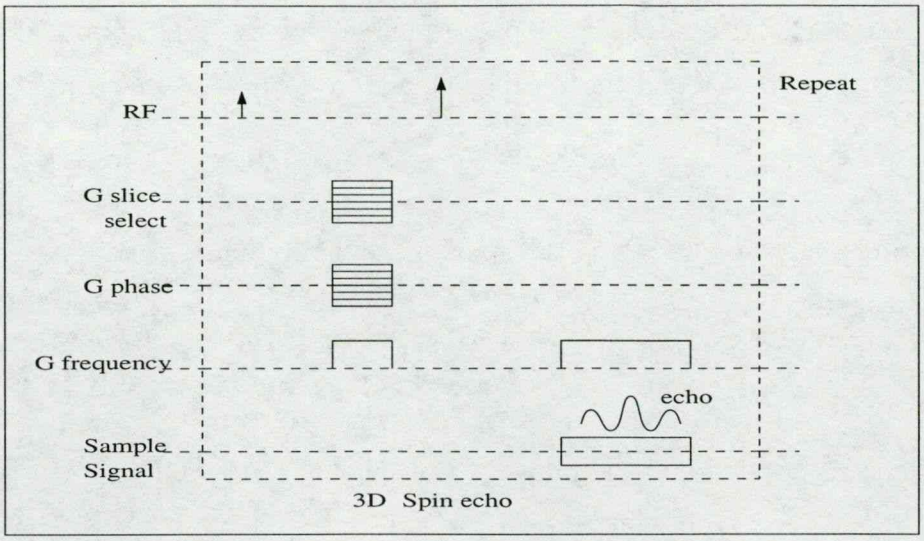

Figure 1.12: 3-D Spin-Echo imaging sequence.

plane. The x, y and z gradients are then turned On to encode the phase of the spins with regard to their spatial position. This is followed by a 180 degree pulse to reverse the phase of the spins and the application of an x gradient during which time the signal is acquired. We will follow the behavior of the magnetization vector during the course of this pulse sequence.

After the 90^o pulse at $t = 0^+$, the spins are in the transverse plane.

$$t = 0^+ : m = m(x, y, z, 0) = m_0. \tag{1.39}$$

During the time interval $0 < t < t_a$, the spins precess under the influence of field inhomogeneities represented by B''.

$$t = t_a : m = m_0 e^{-i\gamma B'' t_a}. \tag{1.40}$$

During the time interval $t_a < t < t_b$, the spins precess under the influence of both the field inhomogeneities given by B'' and the gradients given by $B' = G_x x + G_y y + G_z z$.

$$t = t_b : m = m_0 e^{-i\gamma\ B'' t_b} e^{-i\gamma\ B' \tau}. \tag{1.41}$$

Then, during the time interval $t_b < t < t_c$, the spins precess only under the influence of the field inhomogeneities.

$$t = t_c^- : m = m_0 e^{-i\gamma\ B'' T_I} e^{-i\gamma\ B' \tau}. \tag{1.42}$$

At $t = t_c$, a 180^0 pulse is applied and the phase of the spins is reversed.

$$t = t_c^+ : m = m_0 e^{i\gamma\ B'' T_I} e^{i\gamma\ B' \tau}. \tag{1.43}$$

During the time interval $t_c < t < t_d$, the spins precess under the influence of B'' only.

$$t = t_d : m = m(t_c^+) e^{-i\gamma\ B''(t'+TI)}, \tag{1.44}$$

where $t' = t - TE$. The signal is acquired during the time interval $t_d < t < t_d + 2\tau$ while the x-gradient field is on.

$$m = m(t_c^+) e^{-i\gamma\ B''(t'+TI)} e^{-i\gamma\ G_x x(t'+\tau)} \tag{1.45}$$

$$= (m_0 e^{i\gamma\ B'' TI} e^{i\gamma\ B' \tau}) e^{-i\gamma\ B''(t'+TI)} e^{-i\gamma\ G_x x(t'+\tau)} \tag{1.46}$$

$$= m_0 e^{i\gamma\ B''(TI - t' - TI)} e^{i\gamma\ (G_x x(\tau\ - t' - \tau) + G_y y \tau\ + G_z z \tau)}, \tag{1.47}$$

where the final expression of the magnetization vector is

$$m = m(x, y, z, 0) e^{-i\gamma\ B''(x,y,z)t'} e^{-i\gamma(G_x x t' - G_y y \tau - G_z z \tau)}. \tag{1.48}$$

The total signal from the entire volume can therefore be written as

$$s(t) = \int\int\int\ s(x, y, z) e^{-i\gamma\ B''(x,y,z)t} e^{-(t+TE)/T2} e^{-i\gamma(G_x x t - G_y y \tau - G_z z \tau)} dx dy dz, \tag{1.49}$$

where $s(x, y, z)$ is proportional to $m(x, y, z, 0)$. s(t) corresponds to a 1-D trajectory in k-space.To encode 3-D space, we also vary G_y and G_z and hence we acquire $s(t, G_y, G_z)$. Ignoring both B'' and T2 terms we get:

$$s(t, G_y, G_z) = \int_{x,y,z} s(x, y, z) e^{-i\gamma(G_x x t - G_y y \tau - G_z z \tau)} dx dy dz. \tag{1.50}$$

Making the following change of variables:
$k_x = \gamma G_x t,\ k_y = -\gamma\ G_y \tau,\ k_z = -\gamma\ G_z \tau$ we get

$$s(k_x, k_y, k_z) = \int_{x,y,z} s(x, y, z) e^{-i(k_x x + k_y y + k_z z)} dx dy dz. \tag{1.51}$$

The desired quantity s(x,y,z) is estimated by performing a 3-D Fourier Transform on $s(k_x, k_y, k_z)$.

Upon one excitation, a single line in k-space is acquired by sampling the signal in time with a sampling period equal to $\Delta\ t$, and the acquisition step-size of the x-direction in k-space is given by $\Delta\ k_x = \gamma\ G_x \Delta\ t$. At the end of a period of time equal to TR seconds, the sequence is repeated with G_y changed to a new value and a new line is acquired. The acquisition step size in the y-direction of k-space is given by $\Delta\ k_y = \gamma(\Delta\ G_y)\tau$. For complete 3-D incoding, all of these steps must be repeated with new values of G_z. The acquisition step size in the z-direction of k-space is $\Delta\ k_z = \gamma(\Delta\ G_z)\tau$.

1.3.7 Principle of slice selection

In two-dimensional Fourier MR imaging, the volume of interest is cut into slices that are imaged separately [13]. This is done by selectively exciting a slice of the volume by applying a combination of a frequency-selective RF pulse and a field gradient perpendicular to the plane of the slice. The RF pulse, whose frequency profile is made to be a window of bandwidth $\Delta\omega$, and the amplitude of the slice-selection

gradient, G_z, determine the slice thickness containing the excited protons. This is shown in Fig. 1.13. The center frequency of the RF pulse determines the position

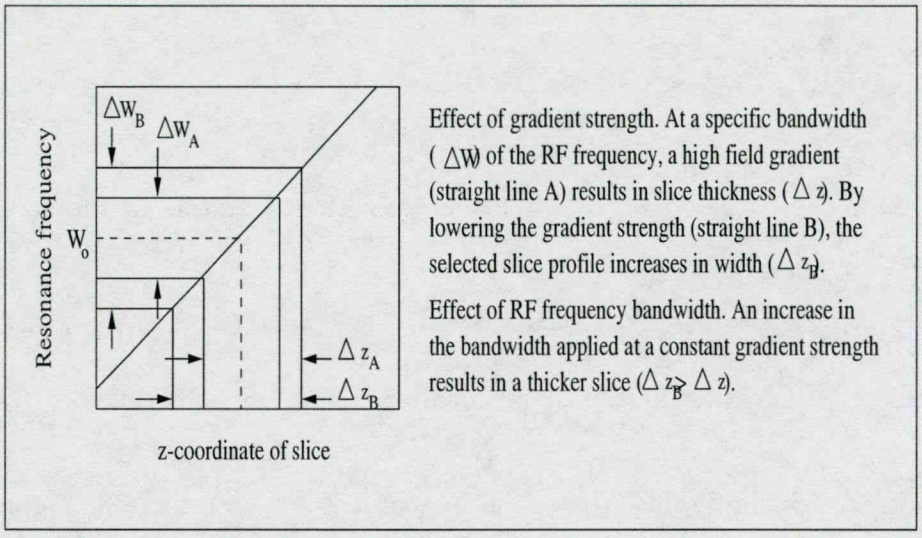

Figure 1.13: Determinants of slice thickness.

of this slice in the imaged volume. The slice thickness, $\Delta\ z$ can be manipulated by varying the gradient strength, the RF bandwidth or both. It is given by the expression

$$\Delta\ z\ =\ \frac{\Delta\omega}{\gamma\ G_z}. \tag{1.52}$$

1.3.8 Contrast manipulation

Image contrast can be manipulated by changing the values of two time parameters of the imaging sequence, TR and TE [4]. The example of a spin echo experiment is used to show the dependence of the signal on TR an TE. Using the solution to the Bloch equations for the longitudinal magnetization (Eq. 1.16), we follow the magnetization vector in a spin echo sequence. After the 90 ^{0} pulse, all magnetization is in the transverse plane,

$$m(t = 0^+) = M_z(t = 0^-). \tag{1.53}$$

Prior to the 180 ^{o} pulse, M_z recovers partially,

$$M_z(t = t_I^-) = M_0(1 - e^{-\frac{T_I}{T1}}), \tag{1.54}$$

and the 180 ^{o} pulse puts M_z along -z.

$$M_z(t = t_I^+) = M_0(e^{-\frac{T_I}{T1}} - 1). \tag{1.55}$$

At the end of the TR period, the longitudinal magnetization available in the next period is as follows,

$$M_z(TR^-) = M_0(e^{-\frac{TI}{T1}} - 1)e^{-\frac{TR-TI}{T1}} + M_0(1 - e^{-\frac{TR-TI}{T1}}) \tag{1.56}$$

$$= M_0(1 - 2e^{-\frac{TR-TI}{T1}} + e^{-\frac{TR}{T1}}). \tag{1.57}$$

The signal density at the time of the spin-echo including the T2 term is

$$s(x, y, z) \propto \ M_0(1 - 2e^{-\frac{TR-TI}{T1}} + e^{-\frac{TR}{TI}})e^{-\frac{TE}{T2}}. \tag{1.58}$$

Normally, TR$\gg$TI and we can write that

$$s(x, y, z) \propto \ (1 - e^{-\frac{TR}{T1}})e^{-\frac{TE}{T2}}. \tag{1.59}$$

Image contrast can be manipulated by varying TR and TE as seen in Eq. 1.59. For example, to get a T2 weighted sequence, we choose TR$\gg$T1 so that

$$s(x, y, z) \propto \ e^{-\frac{TE}{T2}}, \tag{1.60}$$

which depends only on T2. To get a T1 weighted sequence, we choose a short TE and a short TR so that

$$s(x, y, z) \propto \ 1 - e^{-\frac{TR}{T1}}, \tag{1.61}$$

which depends largely on T1. To get a proton density image, we choose a long TR and a short TE. Figure 1.14 shows that by manipulating the values of TR an TE there may even be contrast reversal between different tissues.

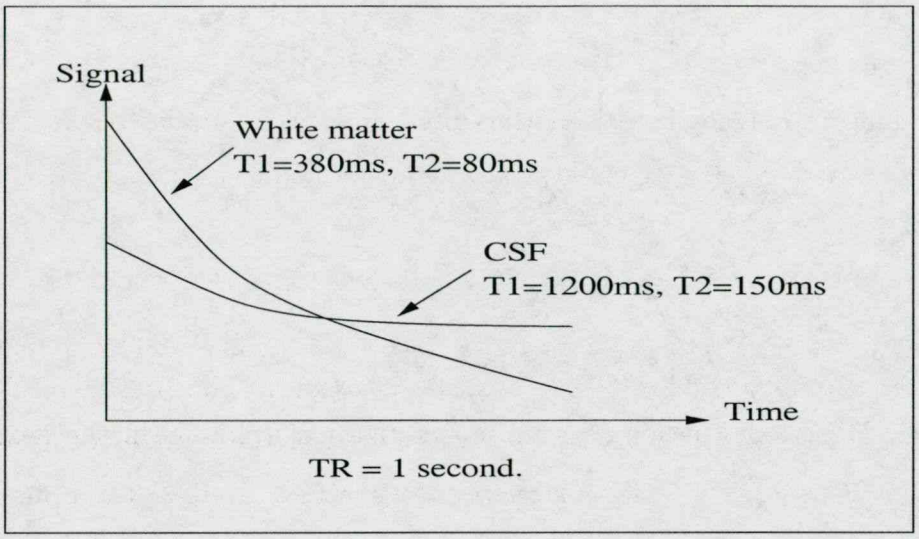

Figure 1.14: Contrast reversal with variable TE.

1.3.9 Signal to Noise Ratio (SNR)

In MR imaging, Signal to Noise Ratio is an important determinant of image quality. Noise can arise from a variety of sources [14] and is superimposed on the MR signal. Its primary sources are the thermal variations of the resistance of both the electrically conductive tissues and the RF receive coil. In a normal MR experiment, temperature can be considered as being constant, and the noise level in the received signal depends on the bandwidth of the receiver. Decreasing this bandwidth contributes to decreasing the level of collected noise. Generally, the receiver bandwidth is also constant for a given imaging experiment.

Practically, increasing the Signal to Noise Ratio can be achieved by increasing the level of the received signal. To increase the received signal level, we can either increase the B field strength or increase voxel size. Increasing the B field has been shown to increase the SNR in tissue imaging by the same amount [15]. However, generally, the magnitude of the B field is a system dependent constant. Since the signal level depends on the number of contributing protons, increasing voxel size

amounts to increasing the signal level and thus SNR. However, spatial resolution is inversely related to voxel size and trade offs have to be made depending on the application.

Averaging over a number of images causes an increase in the SNR [16] due to the fact that the signal sums up linearly, while the noise increases due to its statistical nature only by the square root of the number of observations. The overall result of averaging is an increase in the SNR by the square root of the number of averages. However, averaging requires multiple acquisitions, which decreases temporal resolution.

Image contrast in also affected by the SNR. Pixel values oscillate about a mean determined by the signal, and the range of oscillations is proportional to the noise level. Hence, small differences between adjacent pixels can be obscured due to noise, and since contrast between two regions of an image is the difference in their levels of brightness, more or less contrast can be achieved depending on the SNR.

1.4 Imaging techniques: Pulse sequences

A pulse sequence is the time organization of the ensemble making up the RF excitation, the gradient switchings and the acquisition of the NMR signal. The evolution of the sequence determines the way in which data is encoded and acquired. This evolution is dictated by the imaging algorithm that controls the complete play-out of the pulse sequence. In general, imaging methods employing standard Fourier spatial encoding have an imaging algorithm that characterizes the phase encoding order, the number of echoes per repetition period, and the slice selection strategy. Other methods such as spiral scan imaging [17], or dynamically adaptive techniques [18] have more complex imaging algorithms.

Some imaging techniques like echo-planar imaging [19] consist of a single RF exci-

tation of the imaging plane followed by the totality of gradient switching and sampling periods covering the whole of k-space. Since they only require one excitation, these techniques are other called "single-shot" techniques [20]. Other imaging techniques such as the spin-echo method [21] consist of a repeated period of RF excitation followed by gradient switching and acquisition, requiring multiple excitations to cover k-space and are therefore called "multi-shot" techniques [22]. The Fast spin echo sequence is a combination of multiple excitations, each yielding the acquisition of multiple lines of k-space and is a "hybrid" technique.

Most imaging schemes have a fixed ordering of the data acquisition and their evolution is completely determined regardless of the evolution of the imaged object. They are called "non-adaptive". On the other hand, so called "adaptive" methods have been designed that concentrate on the changing portion of the desired field of view and alter the play-out of the whole sequence in order to best account for that change.

The following gives a brief description of the main pulse sequences in use today.

1.4.1 Spin-Echo

The Spin-echo sequence [21] was described briefly in Section 2.9. It consists of a 90 degree slice selective RF pulse (sinc-shaped to contain a window of frequencies), followed by a rephasing gradient along the slice selection axis (which compensates for dephasing throughout the slice) and dephasing gradients both in the frequency and phase encoding directions. (The strength of the phase encoding gradient is varied for each shot). This is followed by a 180 degree RF pulse with the same slice selection gradient. Finally the readout gradient is turned On along the frequency encoded direction. This sequence is shown in Fig. 1.15. The time parameters TR and TE are manipulated in order to vary contrast. TR is defined as the total time between

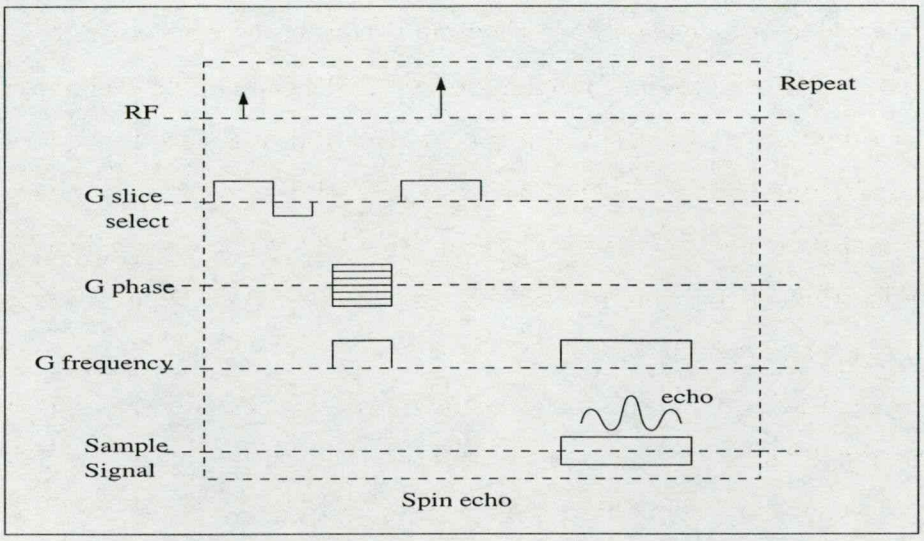

Figure 1.15: Spin Echo sequence.

two 90^o RF pulses and TE indicates the time separating a 90^o pulse from the center of the echo. Depending on the choice of TR, the acquisition of a 256×256 image can take from one to several minutes. Spin echo images are characterized by a high spatial resolution and a very good signal to noise ratio.

1.4.2 2-D Gradient recalled echo

The 2-D Gradient recalled echo sequence [23] is shown in Fig. 1.16. A slice selective gradient is applied simultaneously with a sinc-shaped 90 degree RF pulse. Then, a gradient is applied in the phase encoding direction accompanied by a slice rephasing gradient and a dephasing or 'pre-readout' gradient in the frequency encoded direction. Finally, a rephasing gradient is applied for readout in the frequency encoded direction. The main advantage of the gradient recalled echo sequence is its speed. A typical

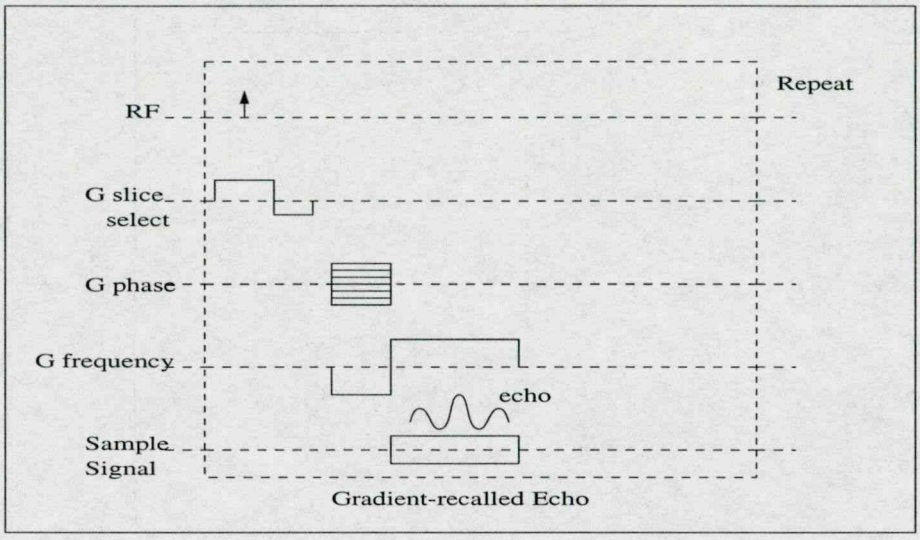

Figure 1.16: Gradient recalled echo pulse sequence.

256 × 256 image takes about 15-30 seconds to acquire. The gradient recalled echo sequence is usually sensitive to T1 because TR is normally quite short. It is also very sensitive to T2* in the frequency encoded direction because spins dephased by static field inhomogeneities are not refocused.

1.4.3 RARE

The RARE (Rapid acquisition with relaxation enhancement) sequence [24] shown in Fig. 1.17 is similar to the spin echo sequence except that each 90^o RF excitation is followed by more than one 180^o refocusing pulse each of which is followed by the acquisition of a separate line of k-space data. The number of 180^o pulses included between two 90 degree pulses is called the echo train length. The main advantage of RARE is the time resolution enhancement over the simple spin echo sequence without

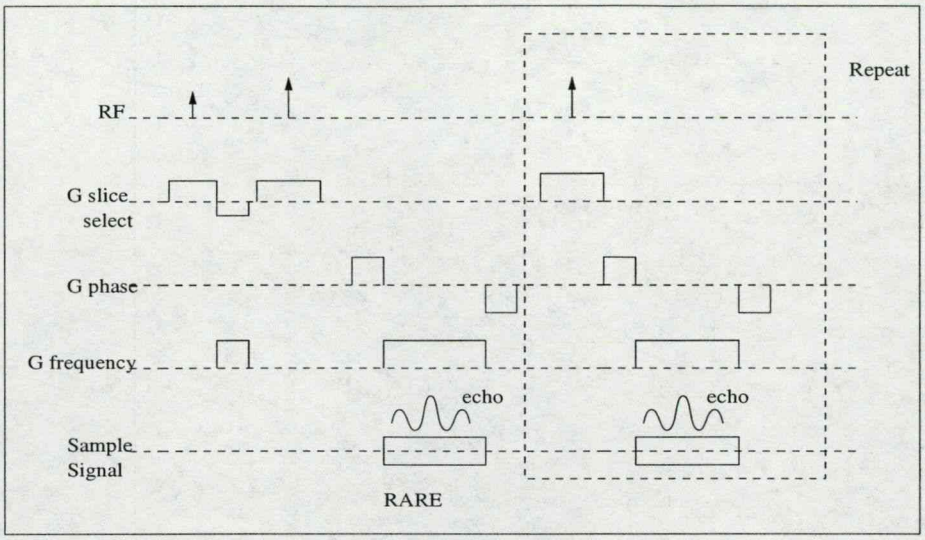

Figure 1.17: The RARE sequence.

any considerable loss in signal to noise ratio. Imaging time is reduced by a factor equal to the echo train length. For an echo train length of 4, several 256×256 images can be obtained in a multi slice acquisition in about 30-60 seconds. A disadvantage of RARE is the increasing T2 dependence on the signal with the increase of the echo train length.

1.4.4 Fast low-flip-angle techniques

The use of lower flip angles permits the choice of a shorter TR without saturation of the magnetization [25], and, consequently image acquisition can be made faster. Low flip angle techniques can be applied to all imaging sequences, however their main drawback is the price paid in Signal to Noise Ratio over the sequences using 90^o flip angles. Typically, for a choice of TR of about 20msec, with an optimal flip angle,

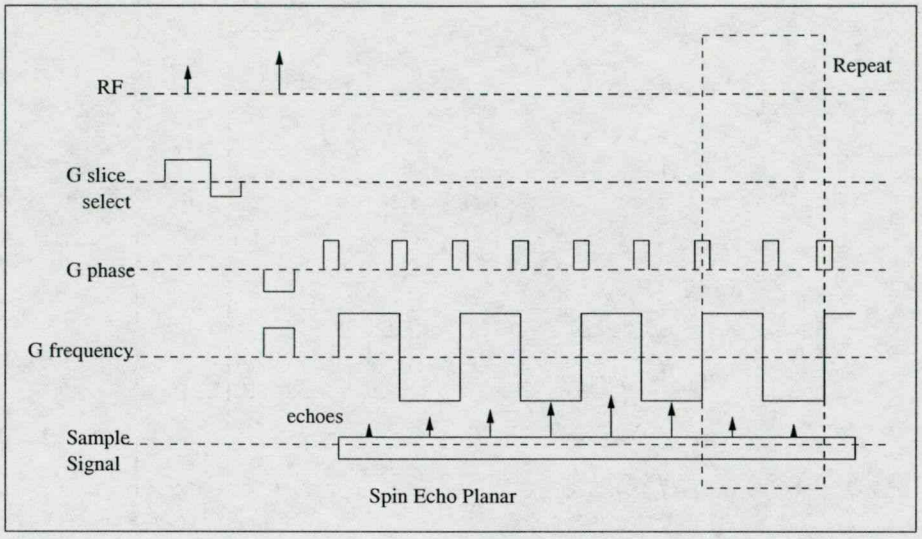

Figure 1.18: 2-D Spin recalled echo planar sequence.

image acquisition time can range from 500ms to a few seconds.

1.4.5 2-D echo planar

The 2-D spin recalled echo planar pulse sequence [19] starts with a selective 90^o RF pulse followed by a rephasing gradient along the slice selection axis. Then, short single simultaneous gradients are applied in both phase and frequency encoded directions, followed by a 180^o RF pulse and a sucession of switchings of the frequency encoding gradient intersecting rapid applications of the phase encoding gradient. Data sampling is performed continuously to acquire a train of multiple echoes. This sequence (shown in Fig. 1.18) is termed "single-shot" since it uses one excitation to fill the desired portion of k-space. The 2-D gradient recalled echo planar sequence [26] shown in Fig. 1.19 is similar to the 2-D spin recalled echo sequence except that it does not have

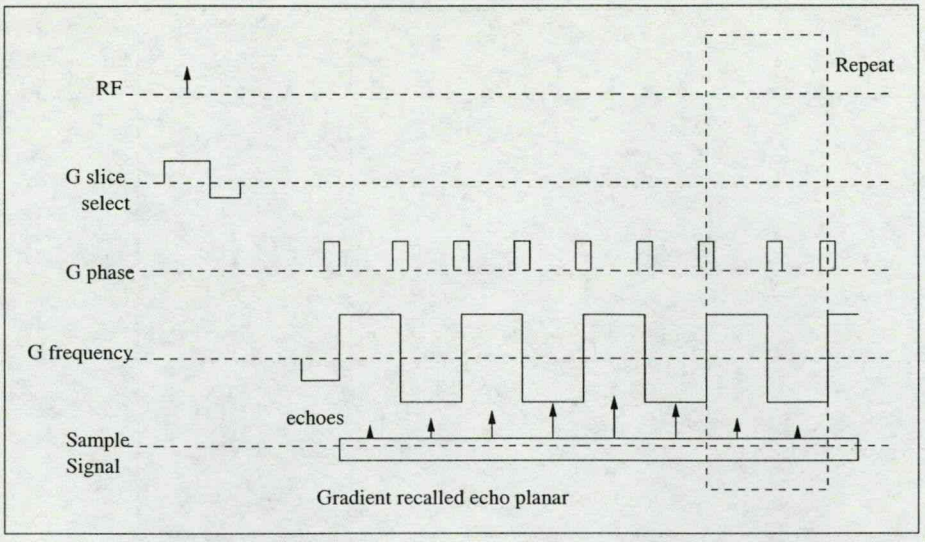

Figure 1.19: 2-D Gradient recalled echo sequence.

a 180^o refocusing pulse. The main advantage of the echo planar imaging techniques is the obvious enhancement in the acquisition time since only one or two RF pulses are required to acquire an entire image which takes between 10 and several hundred milliseconds. Technically however, a number of problems arise in the application of echo planar techniques since they require the use of special fast switching gradient coils (0.1msec) and higher gradient magnitudes (2-3 G/cm). The gradient coils need to be shielded to minimize the induction of Eddy currents. Also, Echo planar techniques are characterized by a low spatial resolution and have a low SNR compared to regular spin echo, gradient echo or RARE. Finally, echo planar images are heavily T2* weighted.

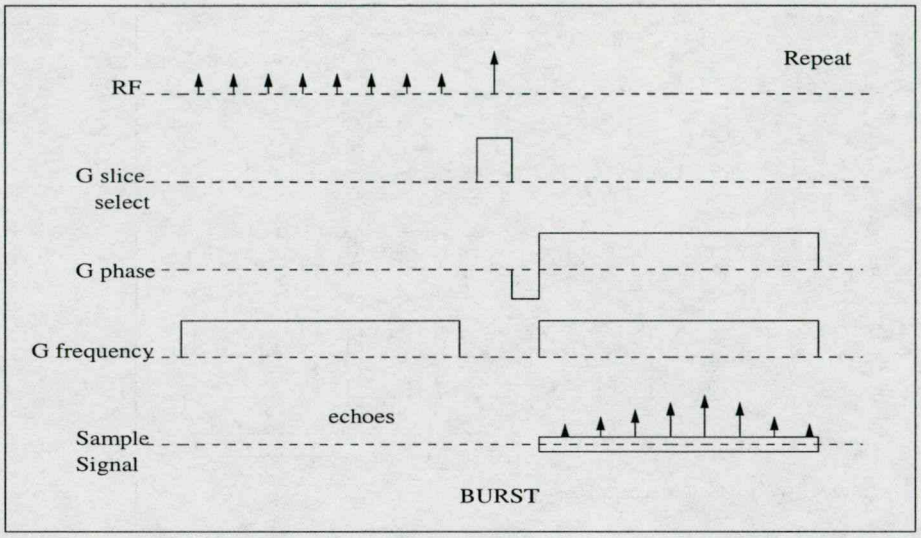

Figure 1.20: The BURST sequence.

1.4.6 BURST

The ultra-fast BURST sequence [27] consists of a rapid sequence of short low-flip angle RF excitations in the presence of a frequency or a phase encoding gradient as shown in Fig. 1.20. These multiple low-flip angle excitations are used to generate multiple echoes which are acquired after the application of a 180^o RF pulse applied with a slice selective gradient. BURST images can be acquired within less than 100msec, however, they have a low SNR. A significant advantage of this sequence is the limited gradient switching.

1.4.7 GRASE

The gradient and spin echo (GRASE) sequence (Fig. 1.21) [28] combines the speed of gradient echo sequences, with a high SNR of spin echo sequences. It starts with

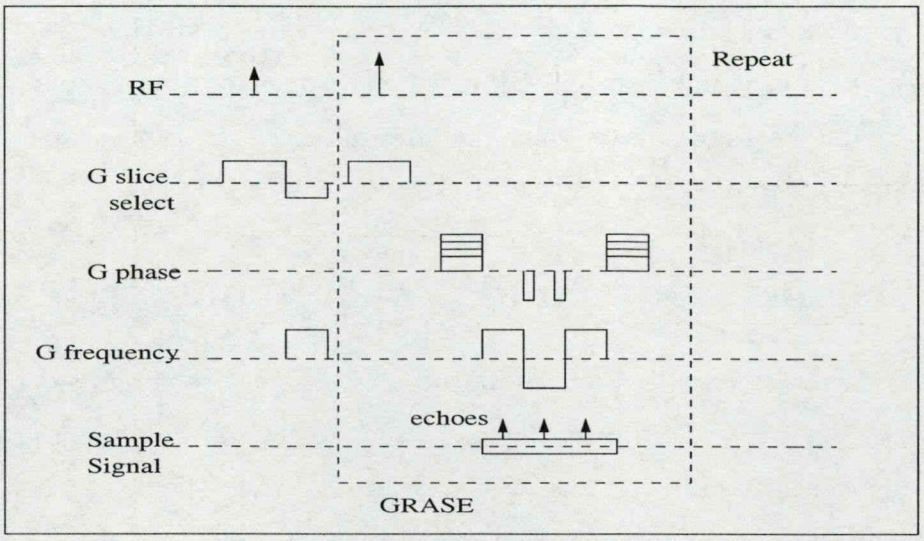

Figure 1.21: The GRASE sequence.

a 90^o RF pulse applied with a slice selection gradient. Following a 180^o refocusing pulse, there is a switching sequence of the phase and frequency encoding gradients along with acquisition of several gradient recalled echoes. Following this, another 180^o RF pulse is applied followed by a new frequency and phase encoding and acquisition sequence. Like RARE, multiple lines of k-space are acquired in a single shot. GRASE images are less affected by field inhomogeneities than those obtained using echo planar sequences and they can be acquired faster than by using fast spin echo.

1.4.8 Keyhole Fourier imaging

Keyhole Fourier imaging [29] reduces the acquired data by sampling only the low-frequency content of the image as it is assumed that the high spatial frequency content of the image is constant. First, an image is constructed using both high and low

frequency phase encoded lines in k-space. Then, dynamic updates are made only of the low-frequency phase encoded lines of k-space. The effect of this reduction in data acquisition is an increase in imaging speed. However, if the assumption that high spatial frequency content of the image is constant does not hold, there is a loss in spatial resolution due to this approach.

1.5 The imaging system and parallel imaging

Although different imaging techniques impose considerably different requirements on the specifications of NMR imager hardware, the major components are common to all techniques [30]. A magnet is used to create a strong uniform magnetic field. Gradient coils provide known and programmable variations in this uniform field. A transmitter delivers RF pulses that induce resonance and an RF coil picks up the NMR signal and delivers it through the receiver to the computer. A computer-based system is provided for control, data acquisition, processing and display functions. Preforming parallel imaging requires the use of multiple RF receiver coils arrayed around the Field Of View (FOV) and receivind data simlutaneously. Next we discuss some background facts governing the performance of RF receiver coils.

1.5.1 RF coils

RF coils are used to transmit and receive RF energy by means of magnetic induction. This energy is spatially dependent on the shape and size of the RF coil being used, and its distribution is dictated by the Maxwell equations []. RF coils are generally designed as circular or rectangular, and are mostly sensitive to spins that are located in their vicinity. The sensitivity distribution is a three-dimensional spatial function that describes the complex weights associated with each point in space, relative to a specified coil. This distribution function depends also on the coupling that the

coils have with the object being imaged [], and determines how the RF energy is distributed spatially when the coil is used to excite; it can be computed from the shape and position of the coil, or experimentally by acquiring an image with that specific coil.

In most MRI applications, RF homogeneity in the FOV is sought. Hence, a large body coil is generally used to excite the spins in the FOV with a constant sensitivity of 1 across the imaged domain. The full k-space image data is then received by one or multiple receiver coils. Parallel imaging requires that the number of receiver coils be greater than one, and that the sensitivity profiles of the coils be spatially variable. For the remainder of this thesis, we will be outline and discuss the performance of a technique of Magnetic Resonance Imaging in parallel. This technique requires the use of a system having multi channel receivers, in order to acquire signal from a number of coils receiving simultaneously. In our implementations, we used a SIGNA GE system having 4 receiver coils, in conjunction with 4-element phased array coils. The specifications of all receivers are considered to be identical, and that the elements in the phased array are electrically decoupled.

Chapter 2

The SPACE RIP method:

2.1 Introduction

Despite the many advances in ultrafast MRI, there is always a need for further increases in the speed of image acquisition. Dynamic imaging applications like cardiac and interventional imaging would be greatly served with an order of magnitude reduction in scan time without sacrificing spatial resolution and signal to noise ratio (SNR). Conventional multi-echo imaging techniques such as RARE and EPI [24] [19], are currently very fast. The new field of parallel imaging can be combined with these methods to further increase imaging speed.

In previous work on parallel imaging, Hutchinson and Raff [31] demonstrated the theoretical feasibility of fast data acquisitions using multiple detectors in MRI. In a subsequent work, Kwiat et al. [32]. investigated methods to solve the inverse source problem on MR signals received in multiple RF receiver coils. Their technique required the use of a number of RF coils equal to the number of pixels in the image, as well as greatly increased receiver coil sensitivities. These requirements are quite impractical in conventional MR imaging where the usual number of pixels in an image is on the order of 256x256, hence the technique was never sucessfully used in medical

imaging.

A number of more promising parallel imaging techniques have been described in the literature [33] [34] [35] which use the sensitivity profiles of RF receiver coils for spatial encoding. Ra et al. [33] described a method that uses sets of equally spaced k-space lines from multiple receiver coils and combines them with sensitivity profile information in order to remove the aliasing that occurs due to the undersampling. A four-fold decrease in the image acquistion time of a water phantom was shown using an array of four coils, though no biological images were shown.

The SMASH method proposed by Sodickson et al. [34] has proven more practical yielding good results in volunteers with clinical implementations. SMASH is designed to enhance imaging speed by using multiple receiver RF coils. It is based on the computation of the sensitivity profiles of the coils in one direction. These profiles are then weighted appropriately and combined linearly in order to form sinusoidal harmonics which are used to generate the k-space lines that are missing due to undersampling. This technique showed an 8-fold increase in imaging speed. SMASH has some inflexibility in the choice of imaging planes due its restriction on the placement of receiver coils along one direction.

The SENSE method proposed by Pruessmann et al. [35] is another parallel imaging technique which relies on the use of 2D sensitivity profile information in order to reduce image acquisition times in MRI. Like SMASH, the cartesian version of SENSE requires the acquisition of equally spaced k-space lines in order to reconstruct sensitivity weighted, aliased versions of the image. The aliasing is then removed with the use of the sensitivity profile information at each pixel. This is done by resolving in the space domain, the linear system of equations obeyed by the intensity of each pixel in the image.

A generalization of SENSE was introduced by Pruessmann et al. [35] which would allow for data to be sampled along arbitrary k-space trajectories. A high compu-

tational cost however accompanies the arbitrary k-space sampling in generalized SENSE methods, currently making reconstruction inconvenient. An elaborate description of the differences between SMASH and SENSE can be found in the SENSE manuscript [35].

In this chapter, we present a parallel imaging and reconstruction technique which attempts to generalize the SMASH approach by allowing for the arbitrary placement of RF receiver coils around the object to be imaged as well as for the use of any combination of k-space lines as opposed to regularly spaced ones. In addition, our reconstruction technique is completely parallel, allowing for real-time rendering possibilities with the use of multiple processors.

2.2 Method

2.2.1 Encoding scheme:

The concept of parallel imaging is based on using multiple receiver coils, with each providing independent information about the image.

The MR signal received in a coil having $W_k(x,y)$ as its complex two-dimensional sensitivity profile, when neglecting all relaxation phenomena, can be written as:

$$s_k(G_y^g, t) = \int\int r(x,y) W_k(x,y) e^{j\gamma(G_x x t + G_y^g y \tau)} dx dy, \tag{2.1}$$

where $r(x,y)$ denotes the proton density function, G_x represents the readout gradient amplitude applied in the x direction, G_y^g represents the phase encoding gradient applied during the g^{th} acquistion, x and y represent the x and y positions respectively, and τ is the pulse width of the phase encoding gradient G_y^g.

In most conventional serial imaging sequences, the readout gradient is constant along one direction, and the phase encoding is applied along an orthogonal direction. In addition, only one receiver coil is used to collect all the data required to reconstruct

a digitized version of $r(x,y)$, with the tacit assumption that $W_k(x,y) = 1$. To achieve this, the phase encoding gradient G_y is varied so as to cover all of k-space with the desired resolution. For each value of G_y^g, an echo is acquired, making serial imaging a time-consuming procedure. In this technique, we use sensitivity profile information from a number of receiver coils in order to minimize the number of acquistions needed to estimate and reconstruct $r(x,y)$. Taking the Fourier transform of Eq.[1] along the x direction when a phase encoding gradient G_y^g has been applied yields:

$$S_k(G_y^g, x) = \int r(x,y) W_k(x,y) e^{j\gamma(G_y^g y\tau)} dy, \tag{2.2}$$

which is the phase modulated projection of the sensitivity weighted image onto the x axis. For the purpose of discretization, we expand $r(x,y)$ and $W_k(x,y)$ along the y direction in terms of a spatially localized set of orthogonal sampling functions $\Omega_n(y)$ to obtain the following equations:

$$r(x,y) = \Sigma_{n=1}^{N} \rho(x,n)\Omega_n(y), \tag{2.3}$$

and,

$$W_k(x,y)e^{j\gamma(G_y^g y\tau)} = \Sigma_{n'=1}^{N} W_k(x,n')e^{j\gamma(G_y^g n'\tau)}\Omega_{n'}(y). \tag{2.4}$$

where N is the number of pixels in the y direction. Combining Eq.[3] and Eq.[4], we get:

$$S_k(G_y^g, x) = \int \Sigma_{n=1}^{N} \rho(x,n)\Omega_n(y) \Sigma_{n'=1}^{N} W_k(x,n')e^{i\gamma(G_y^g n'\tau)}\Omega_{n'}(y)dy \tag{2.5}$$

Rearranging the terms for simplification yields:

$$S_k(G_y^g, x) = \Sigma_{n=1}^{N} \rho(x,n) W_k(x,n')e^{i\gamma(G_y^g n'\tau)} \int \Omega_n(y)\Omega_{n'}(y)dy. \tag{2.6}$$

Since $\Omega(y)$ is orthonormal, we have:

$$\int \Omega_n(y)\Omega_{n'}(y)dy = \delta(n,n'). \tag{2.7}$$

Therefore, Eq.[6] can be written as:

$$S_k(G_y^g, x) = \Sigma_{n=1}^{N} \rho(x,n) W_k(x,n) e^{i\gamma(G_y^g n\tau)}. \tag{2.8}$$

This expression can be converted to matrix form for each position x along the horizontal direction of the image, as follows:

$$\begin{pmatrix} S_1(G_y^1,x) \\ . \\ S_1(G_y^F,x) \\ S_2(G_y^1,x) \\ . \\ S_2(G_y^F,x) \\ . \\ . \\ S_K(G_y^1,x) \\ . \\ S_K(G_y^F,x) \end{pmatrix} = \begin{pmatrix} W_1(x,1)e^{i\gamma(G_y^1 1\tau)} & . & . & . & W_1(x,N)e^{i\gamma(G_y^1 N\tau)} \\ . & . & . & . & . \\ W_1(x,1)e^{i\gamma(G_y^F 1\tau)} & . & . & . & W_1(x,N)e^{i\gamma(G_y^F N\tau)} \\ W_2(x,1)e^{i\gamma(G_y^1 1\tau)} & . & . & . & W_2(x,N)e^{i\gamma(G_y^1 N\tau)} \\ . & . & . & . & . \\ W_2(x,1)e^{i\gamma(G_y^F 1\tau)} & . & . & . & W_2(x,N)e^{i\gamma(G_y^F N\tau)} \\ . & . & . & . & . \\ . & . & . & . & . \\ W_K(x,1)e^{i\gamma(G_y^1 1\tau)} & . & . & . & W_K(x,N)e^{i\gamma(G_y^1 N\tau)} \\ . & . & . & . & . \\ W_K(x,1)e^{i\gamma(G_y^F 1\tau)} & . & . & . & W_K(x,N)e^{i\gamma(G_y^F N\tau)} \end{pmatrix} \cdot \begin{pmatrix} \rho(x,1) \\ \rho(x,2) \\ \rho(x,3) \\ . \\ . \\ . \\ . \\ . \\ \rho(x,N) \end{pmatrix} \tag{2.9}$$

where F is the number of phase encodes used in the experiment, and K is the number of coils.

Equation 2.9 is a matrix equation where the term on the left side of the equality is a KxF element vector containing the F phase encoded values for all K coils. The term on the far right is an N-element vector representing the "image" for one column. The middle term in Eq. 2.9 is a matrix with KxF rows and N columns which is constructed based on the sensitivity profiles and phase encodes used. Hence, this approach is not restricted to the case where KxF = N. Solving Eq. 2.9 for each position along the x axis yields a column by column reconstruction of the image.

Figure 2.1 shows a schematic representation of the reconstruction process. As described above, each column in the image is reconstructed separately. In the case where the image matrix has N rows and M columns, a block of M matrices must be inverted to reconstruct the M columns of the image. The matrices are not necessarily

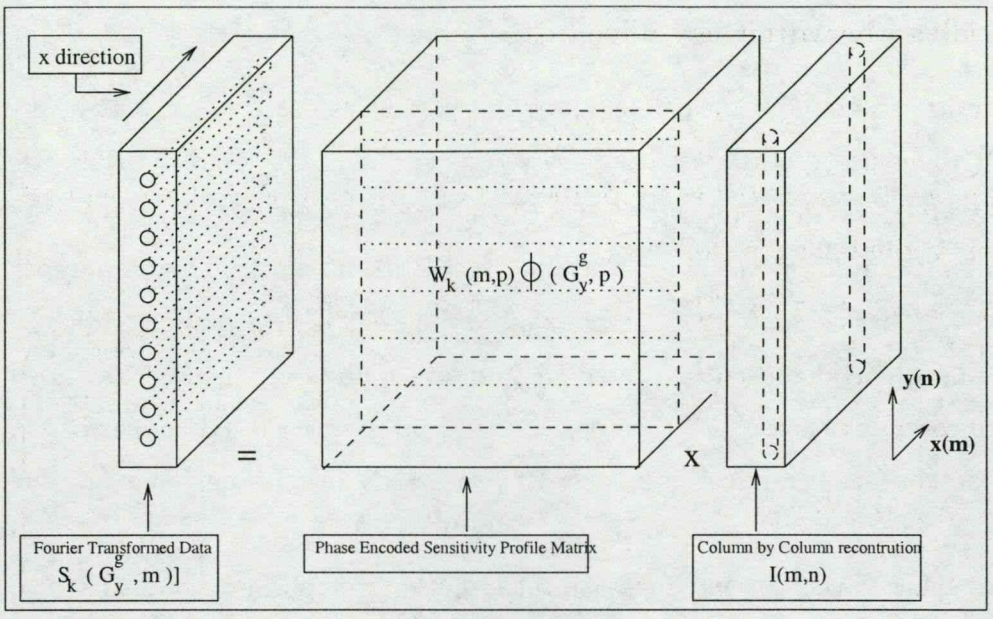

Figure 2.1: Schematic representation of the parallel reconstruction scheme. The matrix to the left represents the 1DFT of the chosen k-space data, the block of matrices in the center is the 3D sensitivity array formed by stacking M 2D matrices such as the one expressed in Eq. 2.9. The matrix on the right represents the image, which is reconstructed column by column by inverting each matrix in the sensitivity array.

square so that a pseudoinverse must be computed for each column. The choice of the number of phase encodes F affects the quality of the reconstruction. Increasing F results in an increase of the rank of the matrices, yielding pseudoinverses that are better conditioned. There is a large computation load associated with this reconstruction, however, the potential for parallelization is obvious, since each column can be reconstructed seperately. For each slice, the pseudoinverses have to be computed only once. Subsequent updates of the same slice can be reconstructed by simple matrix vector multiplication, reducing reconstruction times to real-time rates.

2.2.1.1 Conditioning and the choice of the phase modulations:

The reconstruction scheme outlined in the previous section is based on matrix inversion. In order to insure a stable and robust reconstruction, the condition number of the inverted matrices, defined as the ratio of the largest eigenvalue to the lowest eigenvalue should be minimized [36]. Equation 2.9 shows that the condition number depends on the number of phase encodes F acquired per coil. It is also affected by the choice of the phase encodes used in the acquisition, as well as on the specifications of the receiver coils, which include the sensitivity profiles and the RF penetration. In addition, the condition number is affected by the SNR of the sensitivity profile estimations.

Our results show (Fig 2.6) that increasing the number of phase encodes used in the reconstruction would enhance the conditioning of the reconstruction matrices. To avoid errors due to numerical propagation, the pseudoinverse of each reconstruction matrix is computed after setting a minimum threshold to the eigenvalues. This effectively removes any noise amplification due to bad conditioning. For our reconstructions, we chose a cutoff threshold of 5 percent of the maximum eigenvalue whereby all eigenvalues below that threshold are set to zero and therefore do not contribute to the reconstruction. Our results also show that more RF penetration contributes to better conditioning. Finally, if both the choice of the k-space encodes and the coil penetration are set, the condition number would be expected to depend on the k-space characteristic of the sensitivity profiles of the receiver coils.

2.2.1.2 The k-space coverage:

In order to appropriately cover the k-space of the image $I(x, y)$, the choice of the phase modulations used in the inversion matrix should be determined by the frequency content of the sensitivity profile. In the spatial domain, the image received in a

coil having a sensitivity profile $W_c(x,y)$ can be written as $I_c(x,y) = I(x,y)W_c(x,y)$. In the frequency domain, the k-space profile of $I_c(x,y)$ is the convolution of the k-space profile $I(k_x,k_y)$ of the image $I(x,y)$, with the k-space profile $W_c(k_x,k_y)$ of the sensitivity profile $W_c(x,y)$. This convolution amounts to a blurring of the k-space data $I(k_x,k_y)$ of the image. Since a different convolution is performed for each coil, a different blurring of $I(k_x,k_y)$ occurs at each coil. Subsampling the convolved k-space data received in different coils therefore results in different coverages of the k-space of the image $I(x,y)$. Hence, in order to get the best k-space coverage of the $I(x,y)$ for a given $W_c(x,y)$, it is necessary to optimally sample the k-space data from all the coils.

In contrast to SMASH [34], which requires the use of equally spaced k-space lines, this technique is completely flexible as to that choice. In this work, we use equally spaced k-space lines to demonstrate the technique, and show how more optimal sets of k-space lines can be found to achieve better results. Finding the optimal set of k-space lines is, however, a subject beyond the scope of the current work.

2.2.1.3 Sensitivity profile calculation:

Our method is based on using the sensitivity profiles of RF pickup coils in order to encode MR images. To calculate these profiles, a number of techniques described in the literature could be used [35, 37, 38, 39]. In this chapter, we use a technique that only requires comparison between body coil and surface coil images without any filtering or other numerical manipulations. It was chosen for its simplicity and adaptibility to real-time applications. A baseline image of a homogeneous water phantom is acquired using an RF coil with a homogeneous sensitivity profile covering the whole image. This image can be written as $I(x,y)$. Subsequently, individual images of the same water phantom are acquired using each of the surface coils. The image acquired using the k^{th} coil can be represented as $I(x,y)W_k(x,y)$ where $W_k(x,y)$

is the sensitivity profile of the surface coil. Taking the point by point ratio of the two images yields the sensitivity profile $W_k(x, y)$.

The sensitivity profiles of the receiver coils depend on the loading. We assume that the variation incurred by these profiles amounts to a constant scaling between any two different loads. Therefore, in order to find the sensitivity profile of the receiver coils when loaded with an arbitrary body of interest, we perform a sensitivity profile estimation on that body as described above, then compare it to the sensitivity profiles computed on the homogeneous water phantom in order to extract the scaling factor. The sensitivity profiles calculated from the homogeneous water phantom are then multiplied by the scaling factor and used in the encoding scheme. This is done in order to get maximum coverage of the field of view by the sensitivity profiles. Optimizations of the computed sensitivity profiles by smoothing and interpolation have been proposed in SENSE [35] and may well be used to refine the sensitivity profile estimations in our technique, leading to better conditioned reconstructions.

2.3 3D extension of the SPACE RIP technique

The SPACE RIP technique can be extended to 3D data acquisition strategies and allow for the subsampling of two phase encoded directions. The MR signal received in a coil having $W_k(X, Y, Z)$ as its three-dimensional sensitivity profile, when neglecting T2 decay, can be written as:

$$s_k(G_x^g, G_y^g, G_z^g, t) = \int\int\int \rho(X, Y, Z) W_k(X, Y, Z) e^{i\gamma(G_x^g X t + G_y^g Y \tau_1 + G Z \tau_2)} dX dY dZ \tag{2.10}$$

where t represents time, $\rho(X, Y, Z)$ represents the proton density function, G_x^g is the readout gradient along the x direction, G_y^g and G_z^g are the phase encoding gradients gradient along the y and z directions, all applied during the g^{th} acquistion, γ is the gyromagnetic ratio and τ_1 and τ_2 are the duration of the phase encoding gradients

applied along the y and z directions respectively.

For the purpose of notation, we consider the signal received after slice selection along the Z direction. The MR signal received could then be written as:

$$s_k(G_x^g, G_y^g, t) = \int\int \rho(X,Y) W_k(X,Y) e^{i\gamma(G_x^g X t + G_y^g Y \tau_1)} dX dY \tag{2.11}$$

We seek to represent Equ 2.11 in matrix form by first expressing it as a discrete summation. In order to do that, we perform an expansion of its elements using an orthonormal three- dimensional basis function denoted by $\Omega(X,Y)$ and discretize the time signal to get:

$$s_k = \Sigma_x \Sigma_y \rho(x\Delta s, y\Delta s).W_k(x\Delta s, y\Delta s).e^{i\gamma(G_x^g x \Delta s t + G_y^g y \Delta s \tau_1)} \phi(X,Y) \tag{2.12}$$

where

$$\phi(x,y) = \int\int \Omega(X-x, Y-y) dX dY \tag{2.13}$$

Removing Δs and simplifying Equ.2.12 we get:

$$s_k(G_x^g, G_y^g, T) = s_k^g(T) = \Sigma_x \Sigma_y \rho(x,y).W_k(x,y).e^{i\gamma(G_x^g x T + G_y^g y \tau_1)} \tag{2.14}$$

For the purpose of notation, we call $e^{i\gamma(G_x^g x T + G_y^g y \tau_1)} = \phi^g_{(x,y,T)}$ which is the phase term in equation 2.11 and $W_k(x,y) = W_{(k,x,y)}$. Supposing that the image $\rho(x,y)$ is of dimensions (nxn), and that the time signal $s_k^g(T)$ has m points, equation 2.12 can be written in matrix form by considering $\rho(x,y)$ as a one dimensional vector of length nxn:

$$\begin{pmatrix} s_k^g(1) \\ s_k^g(2) \\ . \\ . \\ s_k^g(m) \end{pmatrix} = \begin{pmatrix} W_{(k,1,1)}.\phi^g_{(1,1,1)} & . & . & . & W_{(k,n,n)}.\phi^g_{(n,n,1)} \\ W_{(k,1,1)}.\phi^g_{(1,1,2)} & . & . & . & W_{(k,n,n)}.\phi^g_{(n,n,2)} \\ . & . & . & . & . \\ . & . & . & . & . \\ W_{(k,1,1)}.\phi^g_{(1,1,m)} & . & . & . & W_{(k,n,n)}.\phi^g_{(n,n,m)} \end{pmatrix} . \begin{pmatrix} \rho(1,1) \\ \rho(1,2) \\ . \\ . \\ \rho(n,n) \end{pmatrix} \tag{2.15}$$

For the g^{th} acquisition, supposing that we have p coils with different sensitivity profiles $(W_1(x,y), W_2(x,y), .., W_p(x,y))$, we can write equation 4 as follows :

$$\begin{pmatrix} s_1^g(1) \\ s_1^g(2) \\ . \\ . \\ s_1^g(m) \\ s_2^g(1) \\ . \\ . \\ s_2^g(m) \\ . \\ . \\ . \\ s_p^g(1) \\ . \\ . \\ s_p^g(m) \end{pmatrix} = \begin{pmatrix} W_{(1,1,1)}.\phi^g_{(1,1,1)} & . & . & . & W_{(1,n,n)}.\phi^g_{(n,n,1)} \\ W_{(1,1,1)}.\phi^g_{(1,1,2)} & . & . & . & W_{(1,n,n)}.\phi^g_{(n,n,2)} \\ . & . & . & . & . \\ . & . & . & . & . \\ W_{(1,1,1)}.\phi^g_{(1,1,m)} & . & . & . & W_{(1,n,n)}.\phi^g_{(n,n,m)} \\ W_{(2,1,1)}.\phi^g_{(1,1,1)} & . & . & . & W_{(2,n,n)}.\phi^g_{(n,n,1)} \\ . & . & . & . & . \\ . & . & . & . & . \\ W_{(2,1,1)}.\phi^g_{(1,1,m)} & . & . & . & W_{(2,n,n)}.\phi^g_{(n,n,m)} \\ . & . & . & . & . \\ . & . & . & . & . \\ . & . & . & . & . \\ W_{(p,1,1)}.\phi^g_{(1,1,1)} & . & . & . & W_{(p,n,n)}.\phi^g_{(n,n,1)} \\ . & . & . & . & . \\ . & . & . & . & . \\ W_{(p,1,1)}.\phi^g_{(1,1,m)} & . & . & . & W_{(p,n,n)}.\phi^g_{(n,n,m)} \end{pmatrix} . \begin{pmatrix} \rho(1,1) \\ \rho(1,2) \\ . \\ . \\ \rho(1,n) \\ \rho(2,1) \\ . \\ . \\ \rho(2,n) \\ . \\ . \\ . \\ \rho(n,1) \\ . \\ . \\ \rho(n,n) \end{pmatrix} \tag{2.16}$$

Equation 5 can be written in a more compact form as:

$$[s] = [W.\phi].[\rho] \tag{2.17}$$

where $[s]$ is the signal vector of size mxp, $[\rho]$ is the image vector of size n^2 and the matrix $[W.\phi]$ represents the encoding matrix which includes the sensitivity profiles of the receiver coils as well as the phase encoding information. The size of $[W.\phi]$ when using one acquisition in all the p coils is (m.p x n^2); it can be augmented by getting more acquisitions with different values of the gradients G_x and G_y. If g acquisitions are used, the size of the vector $[s]$ becomes $m.p.g$ and that of the matrix $[W.\phi]$ becomes (m.p.g x n^2). In order to compute the image vector $[\rho(x,y)]$, the pseudo-inverse of the matrix $[W.\phi]$ needs to be calculated, and multiplied by the data vector $[s]$. This is done by first multiplying both sides of Equ.2.16 by $[W.\phi]^T$:

$$[W.\phi]^T.[s] = [W.\phi]^T.[W.\phi].[\rho(x,y)], \tag{2.18}$$

and solving for $[\rho(x,y)]$:

$$[\rho(x,y)] = ([W.\phi]^T.[W.\phi])^{-1}.[W.\phi]^T.[s]. \tag{2.19}$$

For the sake of simplification, we consider that m=g.p=n. This makes the matrix $[W.\phi]$ square of dimensions (n^2xn^2). The image vector $\rho(x,y)$ can therefore be computed as follows:

$$[\rho(x,y)] = [W.\phi]^{-1}.[s] \tag{2.20}$$

Care should be taken when designing the phase encoding steps in order to insure the invertibility of the matrix $[W.\phi]$. In addition, matrix inversion time reduction techniques should be investigated due to the excessively large size of the matrix.

The previous formulation describes in the most general fashion a way of computing and reconstructing an MR image received in parallel. It remains impractical for applications where real-time display is needed, due to the computer hardware limitations involved when trying to invert a ($64K$x$64K$) matrix needed to get a (256x256) image. In the case where the slice of interest is unchanged, the matrix $[W.\phi]$ is constant, therefore its inverse can be computed prior to the dynamic acquisition and used for all ensuing dynamic updates, reducing the reconstruction time to that of a ($64K$x$64K$) matrix multiplication with a vector of size $64K$. This operation could be accomplished at real-time rates. For other cases, where the slice of interest is dynamically selected, a baseline volume acquisition could be performed and the pseudo-inverse of the matrices $[W.\phi]$ describing all the slices in the volume of interest could be computed prior to the dynamic acquistion, rendering the reconstruction fast enough for real-time applications.

The reconstruction scheme described above handles data in the signal domain and shows the most general case where the phase encoding and readout gradients can be arbitrarily chosen.

2.4 Results

We show the results from a simulation of the method assuming a 16-element coil as well as the results from an experimental implementation of the method with a 4 element array coil. All experiments were performed on 1.5T GE clinical MRI systems operating at either the 5.7 SIGNA or 8.2.5 LX hardware-software configurations.

2.4.1 Simulation results:

2.4.1.1 Noise free, low frequency profiles:

In order to assess the feasibility of the technique under ideal conditions, simulations were performed. We acquired a homogeneous image of a brain, with a matrix size of (256x256), using a head coil, then computed an ideal, noise free sensitivity profile having a $\frac{1}{r^2}$ falloff and a linear phase profile. Its magnitude image is shown in Fig 2.2a, and its phase profile is shown in Fig 2.2b. Then, 16 rotated magnitude sensitivity profiles were computed with an angle of $\frac{2\pi}{16}$ between any adjacent two of them, and given the same phase rofile shown in Fig 2.2b. Next, the computed sensitivity profiles were multiplied point by point with the brain magnitude image in order to get approximations of sensitivity weighted images from surface coils placed at different positions. The sensitivity weighted images are then Fourier transformed in two dimensions in order to get the k-space data. Subsequently, 16 lines of k-space data were taken from each matrix and used to reconstruct the head image. Image matrix size was chosen to be (256x256).

As mentioned in the previous section, the choice of the k-space lines affects the image resolution. In Figs. 2.2 d, e and f, we show three images reconstructed using different sets of k-space data in the KxF = N case. These computations required the inversion of 256 matrices each of size (256x256) and were completed in less than 600 seconds on a SUN UltraSparc machine with a processor speed of 266MHz. These

reconstructions can be performed in less than 1 second if a processor is used for each column and with current processor speeds of over 700 MHz. This represents a clear advantage over the generalized SENSE reconstruction method, especially when the choice of the imaged slice is dynamically changed and a complete calculation of the pseudoinverses is needed. Reconstruction speed increases beyond real-time rates however, when the same slice is being refreshed, and the calculation is reduced to a set of vector matrix multiplications.

Figure 2.2c. shows the reference image reconstructed using a 2DFT on all k-space lines. Figure 2.2d shows a reconstruction using the 16 lines of k-space going between k=-7 and k=8; Figure 2.2e shows a reconstruction using the lines of k-space going between k=-79 to k=80 and skipping 8 lines, and finally, Fig 2.2f shows a reconstruction using the 16 lines of k-space going between k=-127 to k=128 and skipping 16 lines. It can be seen that Fig 2.2e represents the best result of the three, as it shows better resolution than Fig 2.2d, and no artefact as in Fig 2.2f. A certain deterioration of the image is observed in Fig 2.2f as 16 lines are skipped before reconstruction. This suggests that the k-space coverage from such a subsampling is not appropriate.

2.4.2 Experimental results:

Two imaging experiments were done in order to test the performance of the technique in practical situations.

2.4.2.1 Imaging with the cardiac coil:

In the first experiment we imaged a human head using a phased array cardiac coil with 4 elements of size 10cm x 10cm fixed around the FOV. Image matrix size was chosen to be 128x128. First a baseline FSE T2-weighted image was acquired from a homogeneous water phantom using the body coil with TR=2s, TE=102ms and

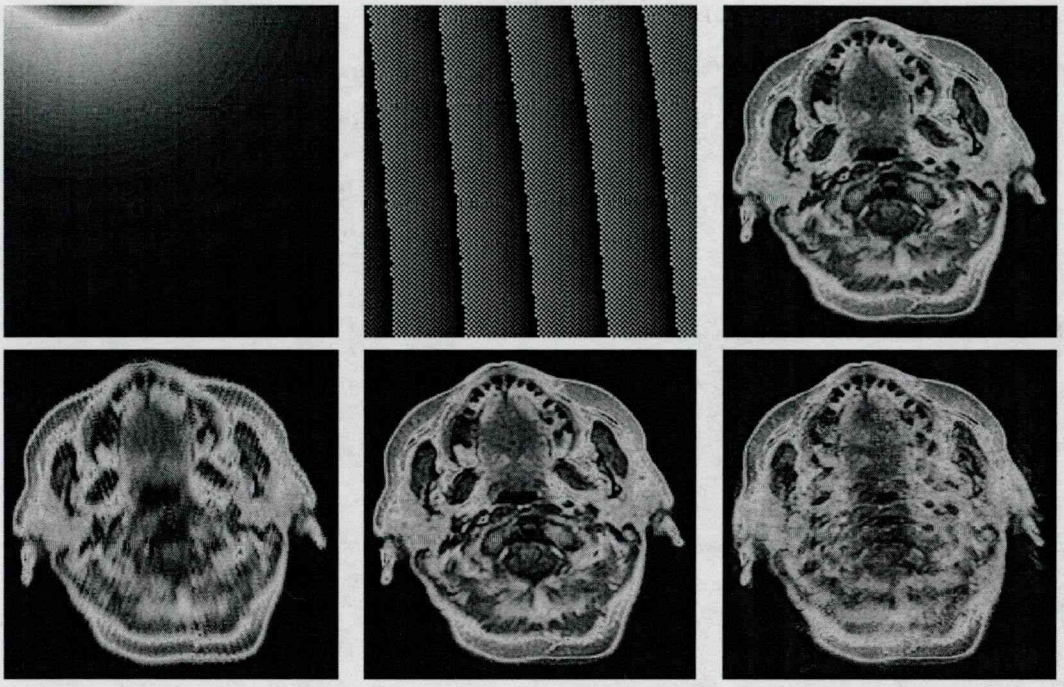

Figure 2.2: Fig 2.2a shows the magnitude of one of the sensitivity profiles used for encoding. Fig 2.2b shows the phase profile used on all sensitivity profiles. Figure 2.2c shows the reference image reconstructed by 2DFT using all k-space lines. Sixteen lines of k-space were used in the simulation assuming 16 coils arranged every 22.5 degrees around the head. Figures 2.2 d, e and f were reconstructed by using the k-space lines acquired from skipping respectively 1, 8 and 16 lines.

ETL=12. Then, the phased array coil was used to simultaneously collect 4 images, one from each coil. These images were used in conjunction with the baseline image to calculate the sensitivity profiles of the coils at different positions using the point by point ratio method as described above. The magnitude images of the sensitivity profiles are shown in Fig 2.3 (top) and their respective phase images are shown below them in Fig 2.3 (middle). Initial calibration was performed in order to remove a linear phase shift which exists between the different coils. This calibration is necessary to insure that the k-space data in all coils is identically centered and that no destructive

interference would arise during reconstruction. This finding is common to all parallel imaging techniques [34, 35] where phase fidelity is crucial for the stability of the reconstructions. The resulting phase images of the adjusted profiles are shown in Fig 2.3 (bottom).

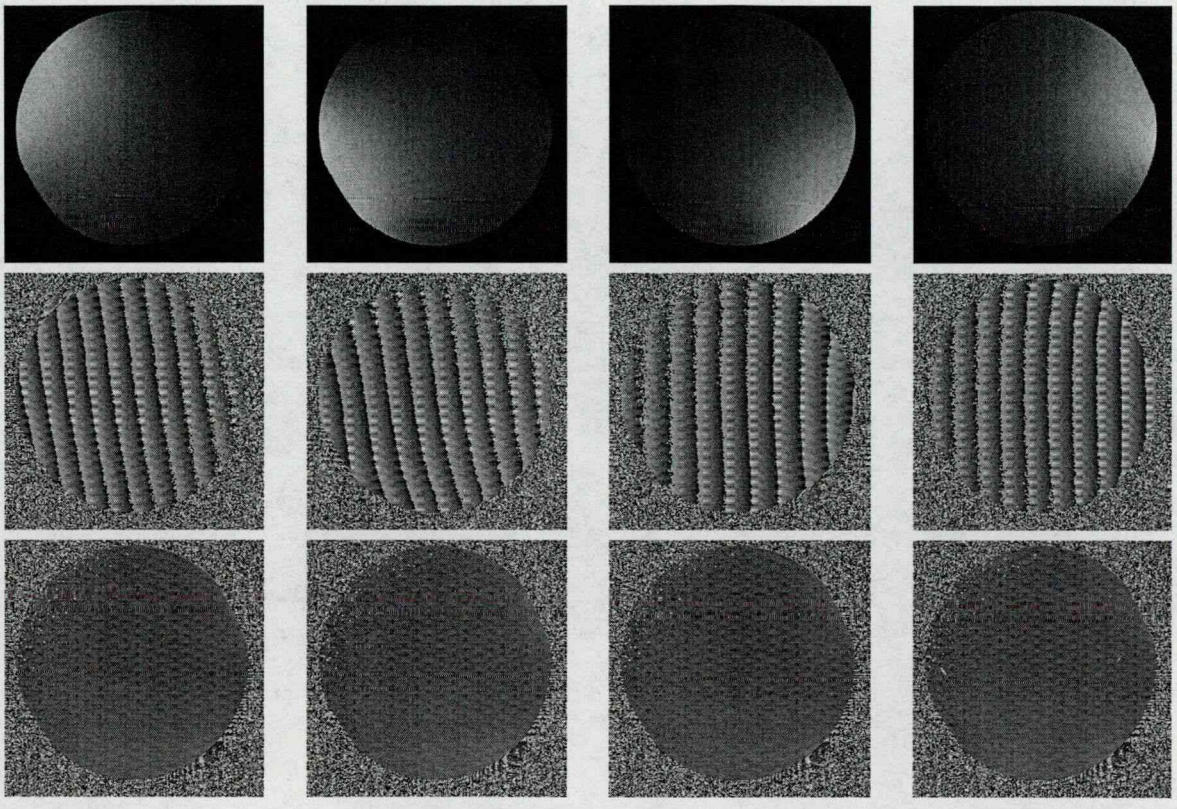

Figure 2.3: Experiment results: The top row shows the magnitude images of the 2D sensitivity profiles as computed from a homogeneous water phantom from all 4 coils in the phased array. The middle row shows the phase images of the sensitivity profiles. The bottom row shows the adjusted phase profiles after linear shifting.

The calibrated profiles were subsequently used to encode a brain image as described previously. In a first reconstruction, we show in the top half of Fig 2.4 the results of this technique, where equally spaced k-space lines were used. Fig 2.4a shows

an image reconstructed using all 128 k-space lines. Fig 2.4b was reconstructed using 64 equally spaced and centered k-space lines, fig 2.4c was reconstructed using 43 k-space lines and Fig 2.4d was reconstructed using 32 k-space lines. Each of these images is shown on top of an image reconstructed by using the same number of k-space lines in the key hole mode [40]. These images are shown respectively in Fig 2.4e, Fig 2.4f, Fig 2.4g and Fig 2.4h.

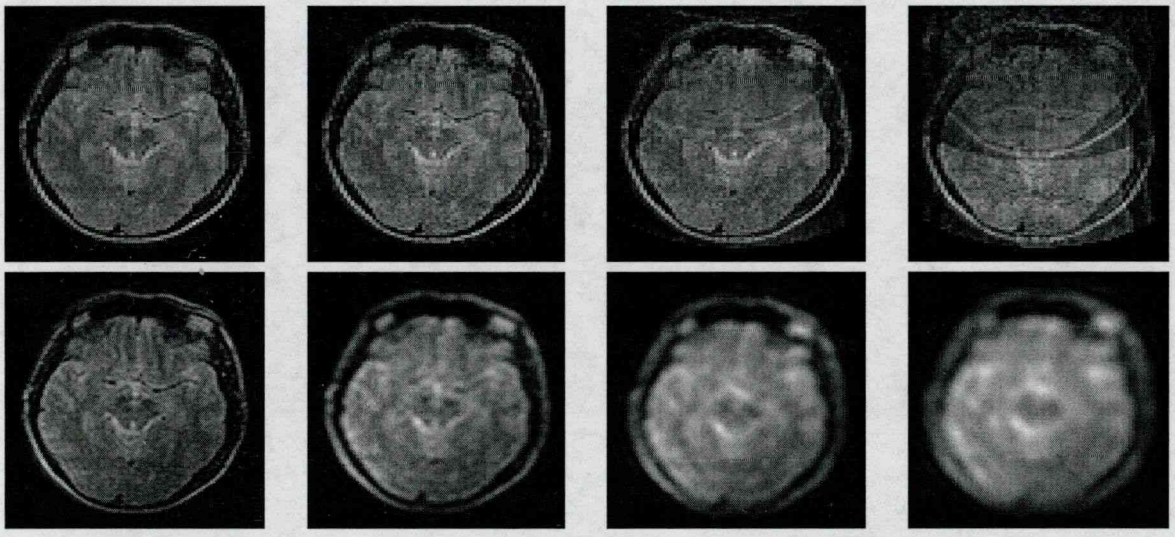

Figure 2.4: Experiment results: The figures on the top show the reconstruction using our technique with the cardiac coil array, and choosing equally spaced k-space lines. The number of k-space lines used are from left to right respectively: 128, 64, 43 and 32. The figures shown on the bottom represent the images obtained by summing the magnitude of the images reconstructed using the middle lines of k-space in all four coils. The number of k-space lines used from left to right are equal to those of the corresponding top figures.

In a second reconstruction, we show the effect of choosing different sets of lines of k-space to enhance the rendering. These results are shown in Fig 2.5 where different sets of 32 lines of k-space are used to reconstruct a brain image. Below each image, we show the lines of k-space that were used to reconstruct it with our technique.

The leftmost image is obtained by using 32 equally spaced lines in k-space whereby the consecutive images are reconstructed by using variations of denser coverages of the center of k-space. Reconstructions were performed on a Sun Ultrasparc station having a processor speed of 266MHz. In all cases, reconstruction times were less than 160s.

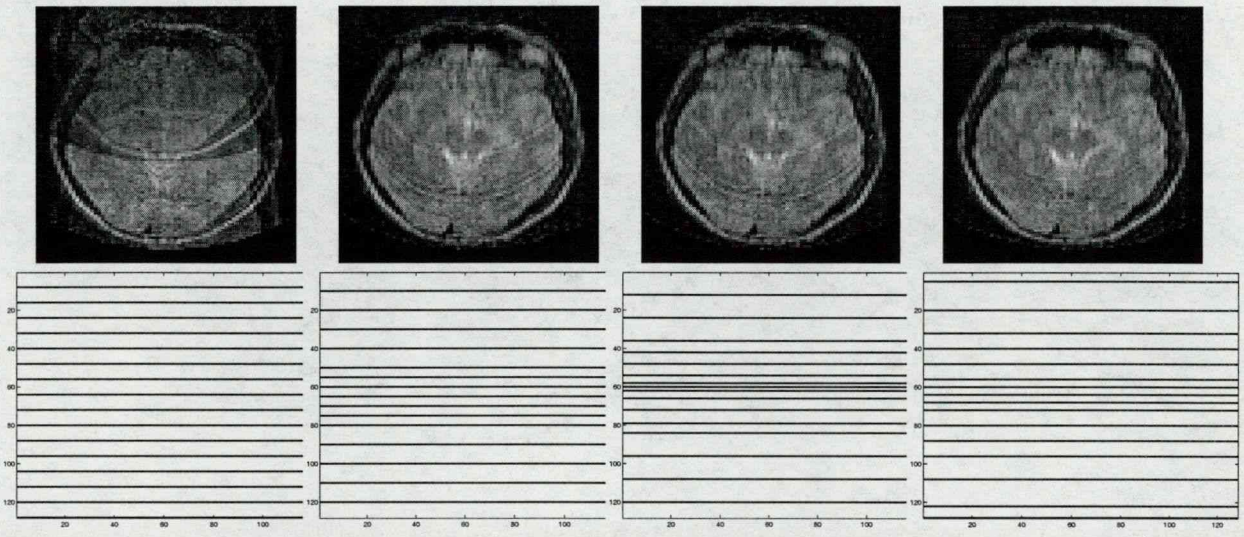

Figure 2.5: Experiment results: The figures on the top show the reconstruction using different sets of 32 lines of k-space with our technique using the cardiac coil array. Below each figure, we show the corresponding k-space lines chosen.

2.4.2.2 Imaging with the torso coil:

In order to test the effect of coil penetration on the reconstruction in practical situations, we repeated the previous experiment (FSE, TR=2s, TE=102ms, ETL=12) using the phased array torso coil with 4 elements of size (15cm x 15cm) fixed around the FOV. Image matrix size was chosen to be (128x128).

In a first reconstruction, we show in the top half of Fig 2.6 the results of this technique, by using equally spaced k-space lines. Fig 2.6a shows an image recon-

structed using all 128 k-space lines, Fig 2.6b was reconstructed by using 64 k-space lines, Fig 2.6c was reconstructed using 43 k-space lines and Fig 2.6d was reconstructed using 32 k-space lines. Each of these images is shown on top of a plot showing the magnitude of the condition number of the reconstruction matrix for every column in the image. It can be seen that the condition number increases when fewer k-space lines are used, hence, a slight overdetermination (KxF > N) is recommended for better reconstructions. We also note that the reconstruction shown in Fig 2.6c contains less artefact than Fig 2.4c due to the larger coil elements. In a second reconstruction,

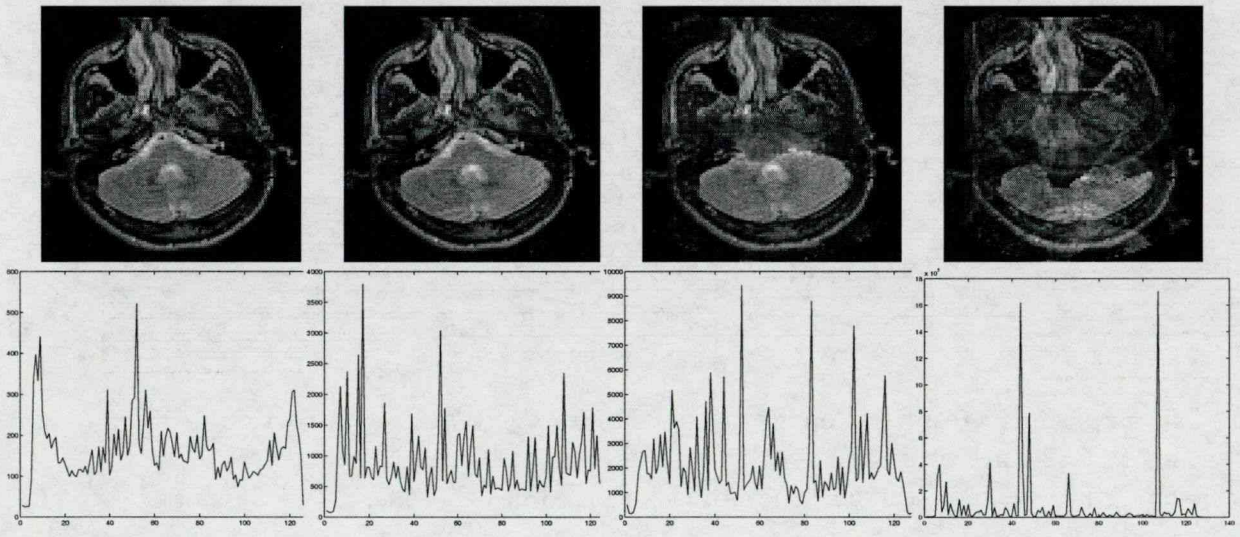

Figure 2.6: Experiment results: The figures on the top show the reconstruction using our technique with the torso coil array and choosing equally spaced k-space lines. The number of k-space lines used are from left to right respectively: 128, 64, 43 and 32. The figures shown on the bottom represent the plot of the condition numbers of the reconstruction matrix for each column. The number of k-space lines used from left to right are equal to those of the corresponding top figures.

we show the effect of choosing different sets of lines of k-space to enhance the rendering. These results are shown in Fig 2.7 where different sets of 32 lines of k-space are used to reconstruct a brain image. Below each image, we show the lines of k-space

that were used to reconstruct it with our technique. The leftmost image is obtained by using 32 equally spaced lines in k-space whereby the consecutive images are reconstructed by using variations of denser coverages of the center of k-space. An overall improvement in image quality is seen compared to the images in Fig 2.5 which we attribute to the greater penetration depth of the sensitivity profiles due to the larger coil elements.

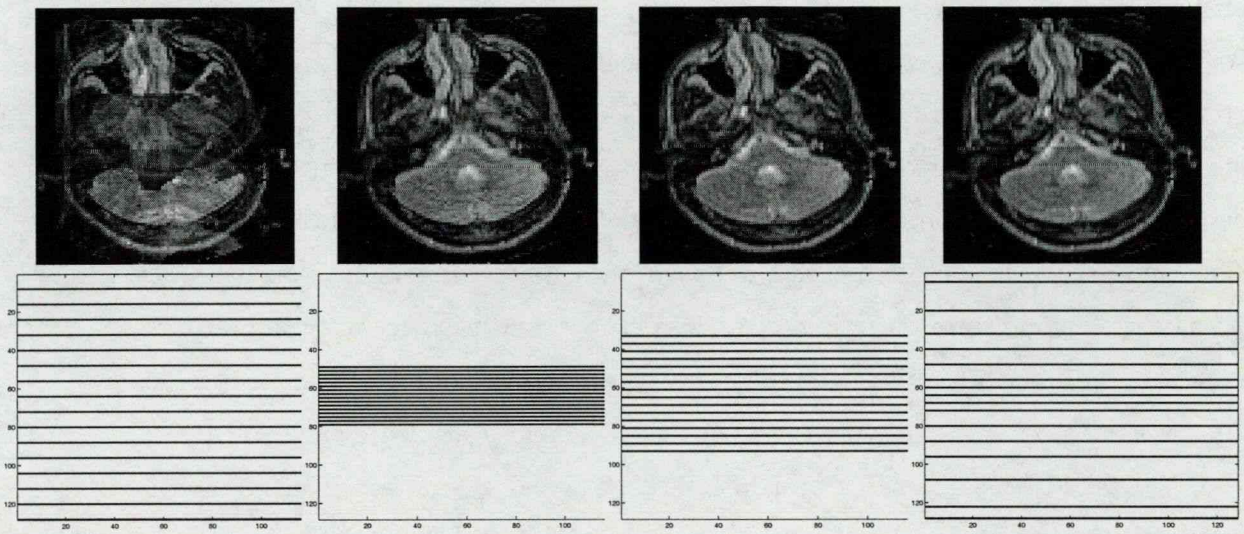

Figure 2.7: Experiment results: The figures on the top show the reconstruction using different sets of 32 lines of k-space with our technique for the torso coil array. Below each figure, we show the corresponding k-space lines chosen.

2.5 Discussion

We have designed and implemented a parallel imaging and reconstruction method intended to complement the SMASH and SENSE techniques. This technique is based on using 2D sensitivity profile maps from an arbitrarily placed array of RF receiver coils, in order to encode and reconstruct MRI data in parallel, therefore reducing

imaging time proportionately to the number of coils present in the array. It is adaptable to any imaging sequence and to arbitrary imaging planes and has the flexibility of being able to use any set of k-space lines for image reconstruction.

The placement of the RF pickup coils can be arbitrary, around the imaged field of view. This allows for the placement of more RF coils than certain parallel imaging techniques such as SMASH [34]. Having more coils in the receiver array would enable faster imaging.

A clear reduction of imaging speed could be achieved using this technique. In this chapter, we show the simulated results of a 16-fold speed increase and experimental results with a four fold speed increase. Since there is a tradeoff between coil size and penetration, an optimal number of coils can be determined to yield the best results.

The reconstruction in this method is based on a matrix inversion algorithm. In order to insure a good reconstruction, our results show that it is necessary to minimize the condition number of the inverted matrices. Better conditioning of the reconstruction matrices can be achieved with the use of more k-space data from each coil (KxF $>$ N) as shown in Figs 2.6e, f, g and h. Once the receiver coil and the number F of acquired k-space lines are chosen, conditioning is achieved by setting a threshold to the eigenvalues in the reconstruction matrix. This is done to minimize numerical propagation errors.

For a given number F of k-space lines used in the reconstruction, our results (Figs 2.5 and 2.7) show that the choice of the phase encodes is crucial to ensure that image resolution is similar to images aquired using full k-space data, and that artefacts due to the regular and insufficient sampling of k-space are eliminated. For all the images shown in Figs 2.5 and 2.7, we found the condition numbers of the reconstruction matrices to be similar, however, the choice of a different set of k-space lines results in dramatically reducing the artefacts.

A current practical limitation of this technique is the need for a large number of

receivers. Most commercial scanners are limited to four receivers, and the high cost of additional receivers makes having as many as sixteen practically prohibitive. This problem could be solved with the use of channel multiplexers [5], whereby multiple coil outputs could be multiplexed and fed into a single receiver and later demultiplexed to get the ouput of each coil.

Our technique is based on the use of coil sensitivity profiles to encode spatial dimensions, therefore, a good estimation of these profiles is crucial to ensure good results. In this chapter, we applied our technique by considering that the sensitivity profiles are independent of the coil loading, allowing us to extrapolate the results of the sensitivity profiles computed from a water phantom to encode other images. In reality however, loading affects the sensitivity profiles of the coil elements and a dynamic method of profile computation would be useful to account for the different objects imaged.

This technique is sensitive to phase differences between coils, which should be accounted for in the reconstruction. Care should be taken to calibrate the data acquisition before the beginning of every imaging experiment.

The reconstruction algorithm presented in this technique allows for the independent computation of each column in the image. This technique therefore lends itself to parallel reconstruction, which can result in realistic image computation times while keeping the flexibility of choosing arbitrary cartesian k-space acquisition trajectories.

We believe that the limitations mentioned are surmountable, and the technique has great potential to overcome the problem of relatively long acquistion times in MRI. The parallel reconstruction algorithm should allow for real-time acquistion as well as reconstruction of MR data and may be very well suited for applications such as cardiac, functional and interventional imaging.

Chapter 3

Artifacts and Signal to Noise Ratio in various k-space sampling strategies

3.1 Introduction

Recent parallel methods in Magnetic Resonance Imaging have shown a great potential in speeding up image acquisition. Two such methods termed SMASH [34] and [35] have been recently applied to cardiac imaging [41, 42] and have shown image acceleration factors of up to six.

The SMASH technique [34] is based on the computation of the sensitivity profiles of the coils in one direction. These profiles are then weighted appropriately in order to form sinusoidal harmonics, which are linearly combined in order to generate all the k-space lines from a small subset of regularly spaced collected ones. SMASH suffers from a few drawbacks such as the inflexibility to choose an arbitrary imaging plane, the limit in the depth of penetration of the RF coils and the limit on the number of coils that can be placed along one direction. In addition, Signal to Noise Ratio (SNR) analysis performed on SMASH reconstructions revealed that the SNR is

inversely proportional to the square root of the acceleration factor, due to the regular sampling of phase encodes.

The SENSE technique [35] uses two-dimensional sensitivity profiles from an array of arbitrarily placed coils, and allows for the use of any k-space trajectory. In its practical version however, SENSE samples k-space regularly, in a cartesian fashion, such as SMASH. This results in aliased images whereby the alising is removed by use of the sensitivity profile information. SNR analysis showed results similar to SMASH when k-space is sampled regularly. When other k-space trajectories are used, image compuation times are still impractical.

More recently, a technique termed SPACE RIP [43] was introduced which allows for the use of multiple RF receiver coils placed arbitrarily around the volume of interest. A random subset of k-space lines could subsequently be used to reconstruct the image. This technique has the advantage of flexibility in the choice of the k-space lines and is amenable to parallel reconstruction making real-time rendering possible.

In this chapter, we apply the SPACE RIP technique to cardiac imaging and show how the choice of the k-space lines used affects the conditioning as well as the SNR of the reconstruction. We show results with a four fold increase in acquisition speed and little loss in the SNR.

3.2 Method

3.2.1 Encoding scheme:

The reconstruction matrix governing the operation of the SPACE RIP technique is based on the use of two-dimensional sensitivity profiles from an array of receiver coils, as basis functions to encode spatial position. When K coils are being used, the reconstruction matrix for each position x along the horizontal direction of the image

is written as follows:

$$\begin{pmatrix} S_1(G_y^1,x) \\ . \\ S_1(G_y^F,x) \\ S_2(G_y^1,x) \\ . \\ S_2(G_y^F,x) \\ . \\ . \\ S_k(G_y^1,x) \\ . \\ S_k(G_y^F,x) \end{pmatrix} = \begin{pmatrix} W_1(x,1)e^{i\gamma(G_y^1 1\tau)} & . & . & . & W_1(x,N)e^{i\gamma(G_y^1 N\tau)} \\ . & . & . & . & . \\ W_1(x,1)e^{i\gamma(G_y^F 1\tau)} & . & . & . & W_1(x,N)e^{i\gamma(G_y^F N\tau)} \\ W_2(x,1)e^{i\gamma(G_y^1 1\tau)} & . & . & . & W_2(x,N)e^{i\gamma(G_y^1 N\tau)} \\ . & . & . & . & . \\ W_2(x,1)e^{i\gamma(G_y^F 1\tau)} & . & . & . & W_2(x,N)e^{i\gamma(G_y^F N\tau)} \\ . & . & . & . & . \\ . & . & . & . & . \\ W_K(x,1)e^{i\gamma(G_y^1 1\tau)} & . & . & . & W_K(x,N)e^{i\gamma(G_y^1 N\tau)} \\ . & . & . & . & . \\ W_K(x,1)e^{i\gamma(G_y^F 1\tau)} & . & . & . & W_K(x,N)e^{i\gamma(G_y^F N\tau)} \end{pmatrix} \cdot \begin{pmatrix} \rho(x,1) \\ \rho(x,2) \\ \rho(x,3) \\ . \\ . \\ . \\ . \\ . \\ \rho(x,N) \end{pmatrix} \tag{3.1}$$

where F is the number of phase encodes used in the experiment, $[W_1,..,W_K]$ represent the sensitivity profiles of the coils, $\rho(x,y)$ represents the image and $[S_1,..,S_K]$ represent the discrete fourier transform of the signals received in all the coils.

Equation 1 is a matrix equation where the term on the left side of the equality is a KxF element vector containing the F phase encoded values for all K coils. The term on the far right is an N-element vector representing the "image" for one column. The middle term in Eq.1 is a matrix with KxF rows and N columns which is constructed based on the sensitivity profiles and phase encodes used. Solving Eq.1 for each position along the x axis yields a column by column reconstruction of the image. Increasing F results in an increase of the rank of the matrices, yielding pseudoinverses that are better conditioned.

3.2.2 SNR and the choice of k-space lines:

In the original SPACE RIP manuscript [43], equally spaced k-space lines were used to demonstrate the technique, and large skips in k-space were shown to result in aliasing artifact due to a poor coverage of k-space. Other distributions of acquired k-space lines were shown to remove the aliasing while maintaining image resolution. In this

work, we show how the energy distribution along the phase encoded direction can be used to pick optimal sets of k-space lines, which would maximize SNR as well as resolution.

The energy distrubution along the phase encoded direction can be computed from an image reconstructed using a full k-space data set, by projecting the magnitude of the k-space data acquired onto the phase axis. This distribution is indicative of the relative amount of energy present at each k-space location along the phase axis, and is typically highest at the center of k-space and decreases as we move towards the edges.

For parallel imaging techniques, where k-space is subsampled in the phase encoded direction, dense sampling in the center of k-space would result in a better preservation of the energy in the image, and consequently a higher SNR than would be achieved through regular sampling. For a fixed number of k-space lines, a dense sampling of the center of k-space comes at the cost of sparse sampling of the edges of k-space. This results in some loss in image resolution, however less significant than the gain incurred, due to the low energy present at high spatial frequencies.

3.2.3 Strategy for choosing the k-space lines:

When acquiring an image of size NxN using one coil, N phase encodes are necessary. Using K coils along with sensitivity profile encoding, the number of phase encodes needed is reduced to $M = \frac{N}{K}$. In order to best cover the energy distrubution, the location of the acquired phase encodes is chosen as follows.

First, a baseline image is acquired using a full set of k-space lines, and the energy along the phase encoded direction is plotted. This energy distribution is then used as a power distribution function to pick random positions for the M acquired phase encodes. These positions are subsequently used to acquire and reconstruct accelerated images. It can be seen that a large number of combinations of k-space lines is possible

using this technique. Our results show a small variability in relative image quality when different sets of k-space lines are used through this method, obviating the need for an exhaustive search for the optimal set.

3.2.4 Quantification of image quality:

In this work, we compare the quality of a number of images reconstructed using different sets of k-space lines acquired to best cover the energy distribution along the phase encoded direction, as described above. To do that, we define two metrics representing relative measures of artefact and resolution in any given image I, given a reference image reconstructed by using the full set of k-space data.

The first of these two metrics is the "quantity of artefact (QOA)" defined as $(I(j) - I_{ref}(j))^2$ where $I(j)$ is a vector formed by reshaping the k-space matrix of the reconstructed image using our technique into a one dimensional array, and $I_{ref}(j)$ is a vector formed by similarly reshaping the k-space matrix of the reference image.

The second metric we use is the "quantity of resolution (QOR)" metric which we define as $\frac{<HI(j), HI_{ref}(j)>}{|HI(j)|^2 . |HI_{ref}|^2}$, where $HI(j)$ is a vector representing a reshaped high-pass filtered k-space matrix of the reconstructed image using our technique, and $HI_{ref}(j)$ is a vector representing a reshaped high-pass filtered k-space matrix of the reference image. A high-pass filter H is used here to enhance the sensitivity of the comparison of the high frequency content and is chosen to be ideal with a cutoff frequency set at 50 percent of the total energy of the image spectrum. This spectrum is computed by projecting the magnitude of the k-space profile of a baseline image onto the phase encoded direction. The baseline image is acquired using a full set of k-space lines and reconstructed conventionally using a 2D Fourier Transform.

The k-space profile is plotted in Fig 3.3e (solid line) along with the filter H (shown by a dashed line). The QOA gives a measure of the atrefact in the reconstructed image and needs to be minimized, whereas the QOR gives a measure of the amount of high

resolution present in the image and needs to be maximized. We combine these two metrics into the "Image Quality Metric (IQM)" such that: $IQM = \frac{QOR}{QOA}$. The IQM is maximized for best image quality.

3.2.5 Computational cost:

Equation 1 governs the reconstruction of the image, and shows how each column can be reconstructed independently. Each reconstructed column is the result of the multiplication of the left-hand side vector of Eq.1 with the inverse of the matrix shown on the right-hand side of the equation. Matrix inversion is computationally expensive, hence, for real-time reconstructions with today's computational capabilities, it is necessary to compute the inverse of the reconstruction matrices before the beginning of the acquisition, which would reduce the computation of each column to a vector-matrix multiplication. The inverse computation would have to be done for each selected slice before the onset of the dynamic acquisition.

3.2.6 Cardiac imaging experiments

In order to assess the SPACE RIP method in a real cardiac imaging situation, we acquired full k-space cardiac data using a cardiac gated EPI sequence, with a 4-element GE cardiac phased array. Image matrix size was chosen to be 128x128. A rigid plastic frame was used to immobilize the elements of the array in order to obtain accurate sensitivity profile estimates of the acquired slices. First, a patient was placed inside the plastic frame and a localizer scan was performed in order to pick the desired slice location. This location was used in subsequent imaging. The top of Fig 3.1 shows a slice reconstructed by adding the magnitudes of the images received in all 4 coils of the chosen slice and at one time point in the cardiac cycle. The patient was then replaced by a homogeneous saline phantom and the same slice

was reacquired in order to get good estimates of the sensitivity profiles at the chosen slice. These are shown in Fig 3.1 bottom.

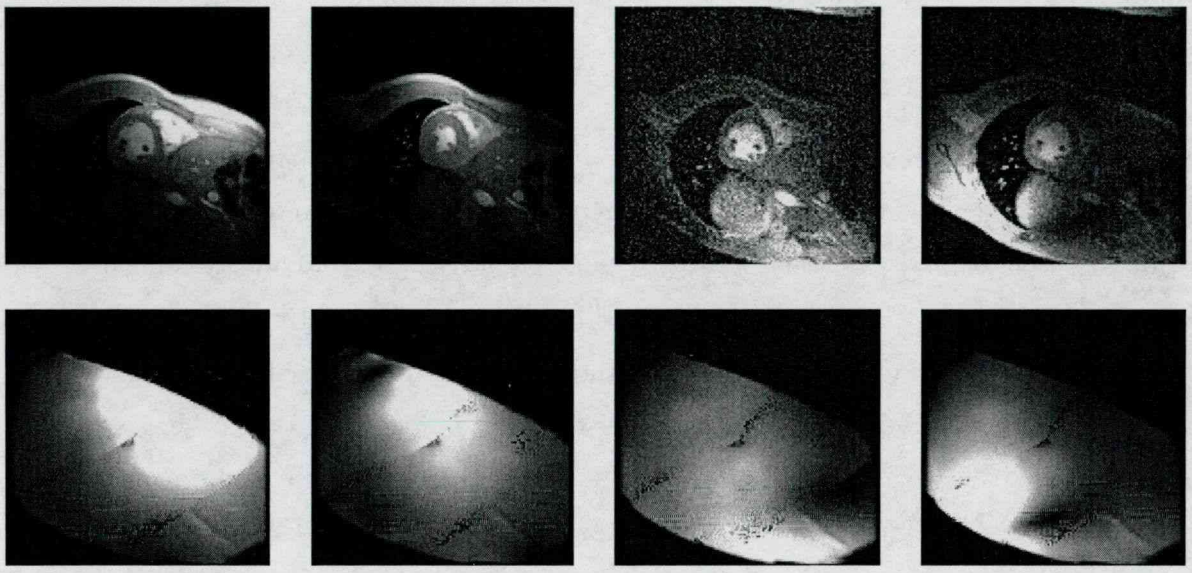

Figure 3.1: The top row shows the chosen slice as acquired with 4 elements in the cardiac phased array; the bottom row shows the corresponding sensitivity profiles from each element in the array.

3.3 Results

3.3.1 Regular k-space sampling:

In a first set of reconstructions, we show at the top of Fig 3.2 the results of this technique using equally spaced k-space lines. From left to right, these images were reconstructed by using respectively, 128, 64, 41 and 32 k-space lines. The corresponding condition numbers for each reconstructed column are plotted below each image at the bottom of Fig 3.2. The SNR values for each of the four images were computed to be 40.1, 22.1, 17.2 and 10.7 respectively. These reconstructions were performed

on a single 266 MHz processor. The computation times were respectively 404, 175, 94 and 85 seconds and were predominantly spent calcualting the inverse of the reconstruction matrices shown in Eq.1. The use of the more current 1 GHz processor reduces these times to approximately 101, 44, 23 and 21 seconds respectively. These times are required each time a new slice is prescribed, (i.e. before the beginning of the dynamic acquisition) and are a function of the image matrix size and the number of k-space lines used. Computation times can be dramatically reduced by the use of multiple processors since each column can be reconstructed independently on a separate processor. Once the inverse of the reconstruction matrix has been calculated, dynamic updates of images could be reconstructed by simple vector-matrix multiplications which can be performed at real-time rates.

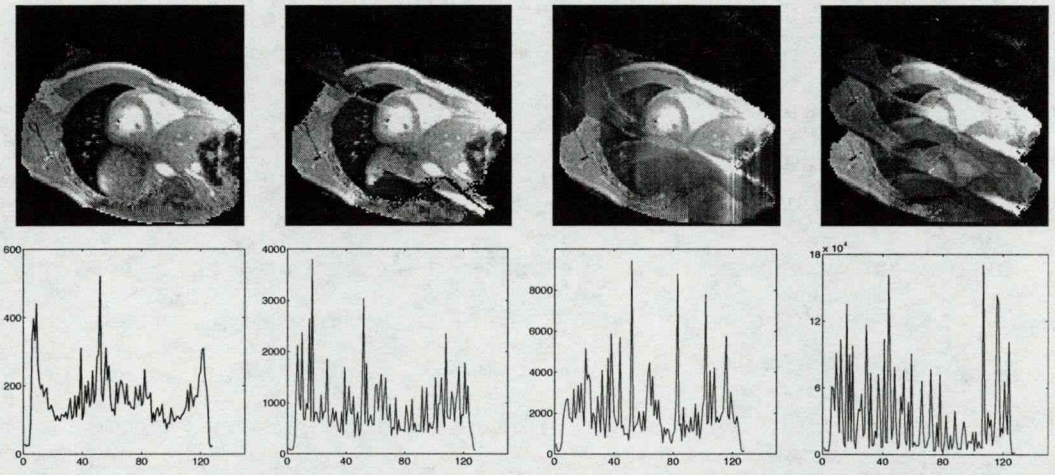

Figure 3.2: Experiment results: The figures on the top show the reconstruction using our technique with the GE cardiac coil array and choosing equally spaced k-space lines. The number of k-space lines used are from left to right respectively: 128, 64, 43 and 32. The figures shown on the bottom represent the plot of the condition numbers of the reconstruction matrix for each column. The number of k-space lines used from left to right are equal to those of the corresponding top figures.

3.3.2 Irregular k-space sampling:

In a second reconstruction, we show the effect of choosing different sets of lines of k-space to enhance the rendering. These results are shown in Fig 3.3 where different sets of 32 lines of k-space are used to reconstruct the same cardiac image. Below each image, we show the lines of k-space that were used to reconstruct it with our technique. obtained by skipping In the bottom-most plot, we show the values of the QOA, QOR and IQM metrics below each corresponding image. Figures 3.3a, 3.3b and 3.3c were reconstructed using regular skips in k-space, whereas Fig 3.3d was reconstructed using a set of k-space lines chosen randomly to fit the energy distribution function. This is done by first computing the energy distribution profile along the phase encoding direction. This profile is shown in the plot Fig 3.3e (solid line) and is used as a probability density function for picking 32 lines of k-space. Half the lines used to reconstruct Fig 3.3d were randomly selected using the energy distribution function for half of the FOV, and replicated symmetrically for the other half; they give the highest value for the IQM metric, suggesting this is the best result we can achieve. This result however is very similar to the reconstruction in Fig 3.3c, and very similiar to other reconstructions we performed using another set of randomly selected lines using the energy distribution. This indicates that any set of k-space lines selected using the energy distribution function may be optimal, eliminating the need for an exhaustive search which is impractical. Additionally, the SNR values for these images, from left to right were calculated to be 10.7, 39.8, 22.1, and 37.5 . This shows that a careful choice of k-space lines could ensure a preservation of the SNR and image resolution, while increasing imaging speed, as shown in Fig 3.3d.

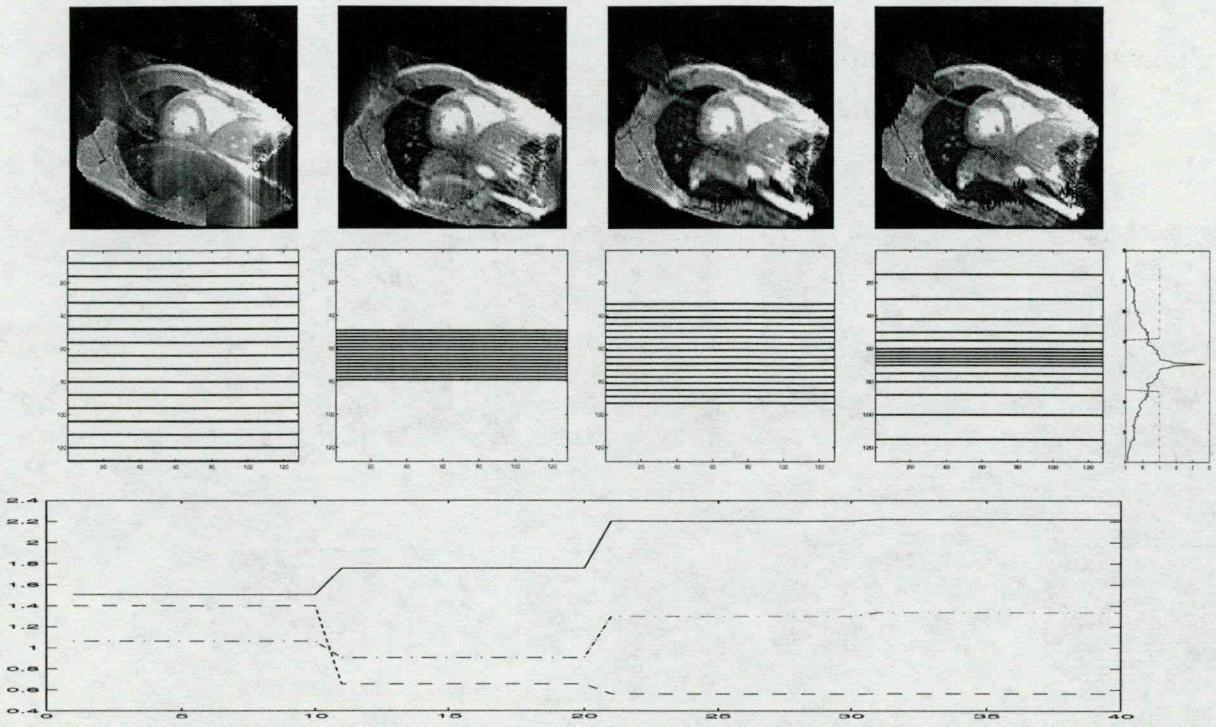

Figure 3.3: Experiment results: The figures on the top show the reconstruction using different sets of 32 lines of k-space with our technique for the cardiac coil array. Below each figure, we show the corresponding k-space lines chosen. In the bottom figure, we show below each set of k-space, the plot of the QOA represented by dashes, the QOR represented by dots and dashes and IQM represented by a continuous line respectively. Figure 3.3e represents the plot of the energy distrubution along the phase encoded direction in continuous line, along with the plot of the high-pass filter H in a dashed line.

3.3.3 Comparison of reconstructions using different k-space sets:

In order to assess the variability of image quality as a function of different randomly selected k-space lines generated to fit the energy distribution, the following reconstructions were performed. Eight k-space sets comprising 32 lines were randomly generated as described in section 2.3 above, and used to reconstruct images following the SPACE RIP method. These reconstructions are shown in Fig 3.4. Our results

show minimal variability in the quality of the reconstructed images, hence, we can conclude that any set of k-space lines randomly selected to fit the energy distribution can be considered as optimal for SNR preservation. Fig 3.2 was used to

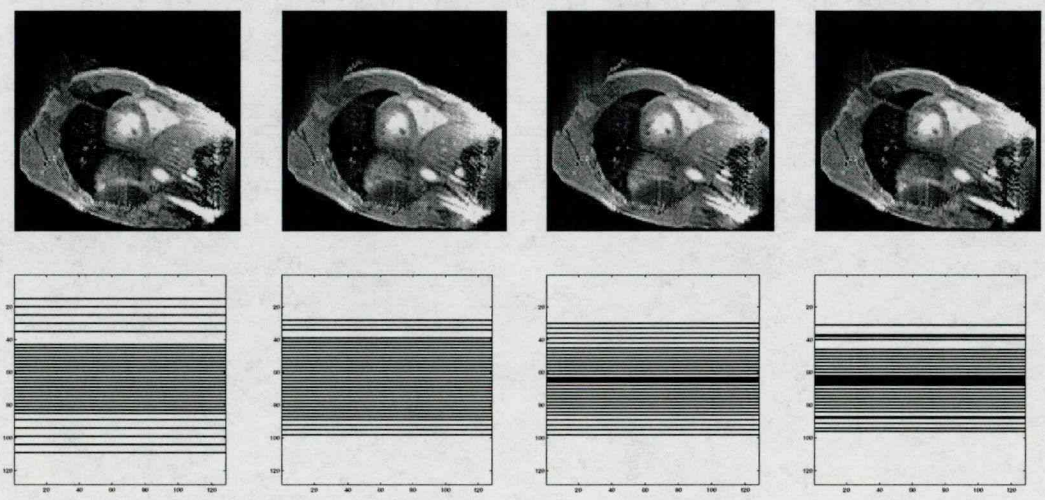

Figure 3.4: The figures on the top show the reconstruction using different sets of k-space lines picked according to the energy distribution along the phase direction. Below each image, we show the k-space lines used to reconstruct it.

3.4 Discussion

We have applied our previously implemented SPACE RIP parallel imaging technique in order to substantially increase imaging speed in cardiac MRI. This technique is based on using 2D sensitivity profile maps from an array of receiver coils in order to encode and reconstruct MRI data in parallel, therefore reducing imaging time by the number of coils present in the array. It allows for the use of an arbitrary set of k-space lines, as well as for the arbitrary placement of the RF receiver coils.

Significant acceleration of imaging speed can be achieved using this technique. In this chapter we show results of a 4-fold speed increase, however, this result can be

enhanced depending on the number of coils that are placed into the receiver array.

The flexibility of the SPACE RIP technique in choosing arbitrary k-space lines was exploited in order to find optimal sets which maximize SNR and resolution. Our results show that the energy distribution profile along the phase encoding direction can be used as a power distribution function for the density of the k-space lines at different positions along that direction, to yield optimal reconstructions.

Two metrics were defined to quantify image quality and were applied to images reconstructed using various sets of optimally chosen k-space lines to fit the energy distribution function. Our results in Fig 3.4 show that little variability in image quality is encountered between these optimal reconstructions obviating the need to search for the optimal set of k-space lines. Hence, any set of k-space lines chosen to fit the energy distribution can be considered as optimal.

Our technique is based on the use of coil sensitivity profiles to encode spatial dimensions, therefore, a good estimation of these profiles is crucial to ensure good results. In this chapter, we applied our technique by considering that the sensitivity profiles are independent of the coil loading, allowing us to extrapolate the results of the sensitivity profiles computed from a water phantom and use them to encode other images. In reality however, loading might affect sensitivity profiles of the coil elements, and a dynamic method of profile computation should be used in order to account for the different objects imaged.

The SPACE RIP technique shows a great potential to overcome the problem of long acquistion times in MRI while preserving SNR and image resolution. The parallel reconstruction algorithm should allow for real-time acquistion as well as reconstruction of MR data, and is very well suited for cardiac imaging.

Chapter 4

Selective Excitation

4.1 Introduction

Despite the many advances in ultrafast MRI, there is still a great need for further increase in the speed of image acquisition. Conventional multi-echo fast methods such as citerare and [19] are being complemented with parallel acquisition strategies whereby multiple RF receiver coils are used to acquire image data. These strategies result in increasing image acquisition speed by an integer factor limited by the number of receiver coils used . Two main parallel techniques termed [34] and [35] have been described in the literature and have shown acceleration factors of up to eight. In both techniques, the SNR was shown to be inversely proportional to the square root of the acceleration factor [34, 35], due to a regular cartesian subsampling of k-space.

The SMASH technique is restricted to regular sampling schemes, and to a linear positioning of the receiver coils. This causes it to have some inflexibility in the choice of the imaging planes, as well as a SNR inversely proportional to the square root of the acceleration factor. The SENSE technique allows for a more general k-space sampling trajectories as well as for a flexible coil positioning. In its practical version however, SENSE requires a regular sampling of k-space, and achieves a SNR that

is inversely proportional to the acceleration factor, such as in SMASH. In addition to its SNR penalty, regular subsampling of k-space, when using large skips in both SMASH and SENSE, results in aliasing in the reconstruction. This is due to the fact that coil sensitivity profiles have low frequency content, and are unable to provide large k-space coverage.

Recently, a new parallel imaging technique termed SPACE RIP [43] was described; it allows for the flexible placement of the receiver coils around the object of interest, as well as to the flexible choice of k-space lines, and is amenable to parallel reconstruction, making real-time image rendering possible. Results from the SPACE RIP technique showed a speed up of image acquisition with little loss to the SNR when the k-space lines acquired are chosen according to the energy distribution of the image, along the phase encoded direction [44], at the expense of image resolution.

In addition, any non-regular subsampling can be used with the generalized version of SENSE. Subsampling can be performed densely in the center of k-space to preserve the SNR and less densely at the periphery, and would achieve similar results as the SPACE RIP technique, albeit with impractical image reconstruction times with today's computational capabilities.

In all parallel imaging techniques to date, the smooth shape of the sensitivity profiles of the receiver coils presents an encoding limitation when high acceleration factors are sought. In this work, we first show how large skips in k-space result in aliasing artifacts (Fig 4.1f) when using sensitivity profile encoding in parallel imaging. We then show how these artifacts can be eliminated with the use of 2D RF selective excitation. Our results show that image acceleration factors well beyond the ones already attained can be achieved without loss in image resolution or SNR, with the acquisition of low frequency phase encodes (Fig 4.3a). Both simulation and experimental results confirm our theoretical expectations.

4.2 Method

4.2.1 Encoding with sensitivity profiles of RF receiver coils:

Parallel imaging requires the use of multiple receiver coils, whereby each coil's sensitivity profile is used as a spatial encoding basis function. When a 2D RF selective excitation profile $S_e(x,y)$ is used to excite an object of interest $\rho(x,y)$, the MR signal received in a coil having $W_k(x,y)$ as its two-dimensional sensitivity profile when neglecting T2 decay can be written as:

$$s_k(t) = \int\int \rho(x,y) W_k(x,y) S_e(x,y) e^{i\gamma(G_x x t + G_y y \tau)} dx dy \tag{4.1}$$

Where $\rho(x,y)$ denotes the proton density function, G_x represents the readout gradient amplitude applied in the x direction, G_y^g represents the phase encoding gradient applied during the g^{th} acquistion, x and y represent the x and y positions respectively, and τ is the pulse width of the phase encoding gradient G_y^g. Generally, selective RF excitation is not used, and $S_e(x,y) = 1$ for all pixels in the image. In most conventional serial imaging sequences, the readout gradient is constant along one direction, and the phase encoding is applied along an orthogonal direction. In addition, only one receiver coil is used to collect all the data required to reconstruct $\rho(x,y)$, with the tacit assumption that $W_k(x,y) = 1$. To achieve this, the phase encoding gradient G_y is varied so as to cover all of k-space with the desired resolution. For each value of G_y^g, an echo is acquired, making serial imaging a time-consuming procedure.

In parallel imaging, sensitivity profile information from a number of receiver coils is used, in order to minimize the number of acquisitions needed to estimate and reconstruct $\rho(x,y)$. A subset of k-space data is collected in each of the coils simultaneously, and combined with the sensitivity profiles in order to reconstruct the image.

4.2.2 K-space coverage:

In order to appropriately cover the k-space distribution of the image $I(x, y)$, the choice of the phase modulations used in the inversion matrix should be influenced by the frequency content of the sensitivity profile. In the spatial domain, the image received in a coil having a sensitivity profile $W_c(x, y)$ following a selective excitation $S_e(x, y)$ can be written as $I_c(x, y) = I(x, y)W_c(x, y)S_e(x, y)$. Therefore, in the frequency domain, the k-space profile of $I_c(x, y)$ is the convolution of the k-space profile $I(k_x, k_y)$ of the image $I(x, y)$, with the k-space profile $W_c(k_x, k_y)$ of the sensitivity profile $W_c(x, y)$, followed by the convolution of the result with the k-space profile $S_e(k_x, k_y)$ of the RF selective excitation $S_e(x, y)$. This convolution amounts to a blurring of the k-space data $I(k_x, k_y)$ of the image. Since a different convolution is performed for each coil, a different blurring of $I(k_x, k_y)$ occurs at each coil. Subsampling the convolved k-space data received in different coils therefore results in different coverages of the k-space of the image $I(x, y)$.

In all parallel imaging techniques, when a regular subsampling of phase encodes is performed in different coils, different parts of the k-space of the image are covered in each of the coils. Aliasing may occur in the reconstruction, if the sensitivity profiles of the coils are similar, or when the spreading of k-space information by the coil sensitivity profiles is insufficient to appropriately cover k-space, as shown in Fig 4.1.

4.2.3 Selective excitation:

Insuring a complete coverage of k-space can be achieved efficiently with the use of selective excitation. Our simulation results (Fig 4.3) demonstrate that high frequency spatial information in the image can be captured by sampling low frequency phase encodes following high frequency selective excitation. This is due to the fact that selective excitation contributes to increasing the extent of blurring in k-space as a

result of the convolution with the k-space profile of the sensitivity profiles, as discussed in the previous section. This in effect mixes spatial frequency information from a large part of k-space into each acquired phase encode, resulting in a better coverage of k-space than would be achieved when selective excitation is not used. Hence, image resolution as well as SNR could theoretically be preserved in SPACE RIP imaging, when sampling low frequency phase encodes following a carefully designed selective excitation. In practice, Panych et al showed that achieving a selective excitation profile containing sharp edges requires the use of lengthy RF pulses [45], which translates into a lengthening of the echo time TE of the pulse sequence. The effect of this lengthening is to slow down the imaging process for short TR sequences as well as to decrease the level of the collected signal due to relaxation in general. This can be avoided by the use of smoother selective excitation profiles which can be applied in a relatively short time but will result in less efficient k-space dissipation, requiring the need to sample high frequency phase encodes to ensure full k-space coverage as will be shown in Fig 4.4.

4.2.4 Conditioning of the reconstruction matrix:

The reconstruction schemes for the SENSE and SPACE RIP methods are based on matrix inversion. In order to insure a stable and robust reconstruction, the condition number of the inverted matrices, defined as the ratio of the largest eigenvalue to the lowest eigenvalue should be minimized [36]. Equation 4 shows that the condition number is dependent on the choice of the phase encodes F acquired per coil; it is also a function of the sensitivity profile estimations of the receiver coils, which depend on the shape, size and position of the receiver coil array. Since the sensitivity profiles are coil dependent, and generally fixed, conditioning the reconstruction of the SPACE RIP technique is practically performed by carefully choosing the k-space lines acquired. The addition of selective excitation profiles $S_e(x, y)$ provides added

flexibility in the conditioning of the reconstruction matrix, since it is equivalent to shaping the sensitivity profiles of the receiver coils $W_k(x, y)$.
The SNR in the resulting images is also a function of the condition number of the reconstruction matrix shown in Eq.4. To avoid errors due to numerical propagation, the pseudoinverse of each reconstruction matrix is computed after setting a minimum threshold to the eigenvalues. This effectively removes any noise amplification due to poor conditioning.

4.2.5 Pulse sequence design

We implemented a general multi-shot multi-echo pulse sequence on the GE Signa 1.5T system, that would allow for any RF excitation sequence to be entered and played out at the beginning of the experiment, as a binary file. This sequence allows for the testing of any variety of selective excitation profiles. The 2D selective excitation profile shown in Figs 4.2a and 4.4a can be implemented by use of a multi-shot gradient echo sequence as shown in Fig ?? left. The RF excitation part of the sequence selects 2D profiles such as the ones shown in Figs.2b and 4b. For each shot, the excitation profile would be shifted down by a fraction of the Field-of-View, and a train of N gradient recalled echoes would be phase encoded and collected in each of the 4 coils, to be used in the reconstruction. Therefore, in order to reconstruct a (128x128) image, it is necessary to excite the system with M shots such as NxMx4=128 or M=$\frac{32}{N}$.

4.2.6 Computational cost

Equation 4 governs the reconstruction of the image, and shows how each column can be reconstructed independently. Each reconstructed column is the result of the multiplication of the left-hand side vector of Eq.4 with the inverse of the matrix shown on the right-hand side of the equation. Matrix inversion is computationally expen-

sive, hence, for real-time reconstructions with today's computational capabilities, it is necessary to compute the inverse of the reconstruction matrices before the beginning of the acquisition, which would reduce the computation of each column to a vector-matrix multiplication. The inverse computation would have to be done for each selected slice before the onset of the dynamic acquisition.

4.2.7 Sensitivity profile calculation

This technique is based on the use of coil sensitivity profiles to encode spatial dimensions. Therefore, a robust estimation of these profiles is crucial to ensure good results. A number of techniques have been described in the literature that allow for the computation of the sensitivity profiles of receiver coils [34, 35]. Our results show [44] that the SNR level of the sensitivity profile estimations greatly affects the reconstruction. We plan to estimate these profiles by averaging in each element of the array, 20 spin-echo acquisitions of a homogeneous saline phantom, completely filling the FOV. This ensures that every point in the space where the object of interest will be placed has a sensitivity estimate; it would also eliminate reconstruction problems due to edges which may be present in the sensitivity profile estimation if computed directly on the object being imaged as encountered by Pruessmann et. al [35]. In our technique, we use the sensitivity profiles computed on a homogeneous saline phantom to encode subsequent images, however, alternative techniques described in the literature for sensitivity profile estimation citesmash,sense may also be used.

4.3 Results

Experiments were performed on a 1.5T GE SIGNA clinical MRI system at the LX 8.2.5 hardware-software configuration. We carried out two sets of experiments to test the performance of our method. In both experiments, image resolution was 256x256

pixels. A 16-echo RARE sequence, TR=2sec, TE=10ms per shot, obtaining one dynamic image update with a single shot.

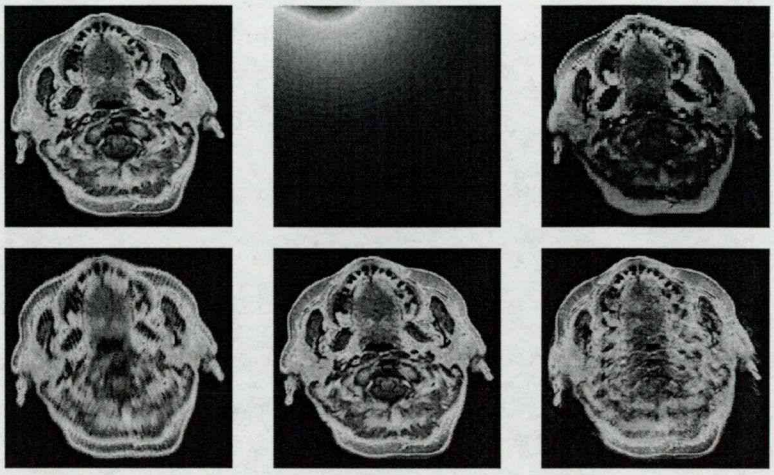

Figure 4.1: Figure 4.1a shows the reference image reconstructed by 2DFT using all k-space lines. Fig 4.1b shows the magnitude of one of the sensitivity profiles used for encoding. Figure 4.1c shows the pixel by pixel product of the reference image with the sensitivity profile to simulate the image acquired by the surface coil. Sixteen lines of k-space were used in the simulations assuming 16 coils. The coils were arranged every 22.5 degrees around the head for Figs 1d,1e and 1f. Figures 4.1d, 4.1e and 4.1f were reconstructed by using the k-space lines acquired from skipping respectively 1, 8 and 16 lines.

4.3.1 Simulation results:

1. Without selective excitation:

In order to assess the feasibility of the technique, simulations were performed on a spin-echo brain image shown in Fig 4.1a. We computed an ideal, noise free sensitivity profile having a $\frac{1}{r^2}$ falloff. This profile is shown in Fig 4.1b. In a first simulation, 16 rotated sensitivity profiles were computed with an angle of $\frac{2\pi}{16}$ inter-coil separation. Next, the computed sensitivity profiles were multiplied pixel by pixel with the brain

image in order to get approximations of sensitivity weighted images from surface coils placed at different positions around the FOV. Figure 4.1c shows the result of the pixel by pixel multiplication of Figs 4.1a and 4.1b. The sensitivity weighted images were then Fourier transformed in two dimensions in order to get the k-space data. Subsequently, 16 lines of k-space data were taken from each matrix and used to reconstruct the head image using our technique.

As mentioned in the previous section, the choice of the k-space lines affects the image resolution. In fig 4.1, we show three images reconstructed using different sets of k-space data. Figure 4.1d shows a reconstruction using the 16 lines of k-space between k=-7 and k=8; Figure 4.1e shows a reconstruction using the 16 lines of k-space between k=-39 and k=40 and skipping 5 lines. Figure 4.1f shows a reconstruction using the 16 lines of k-space between k=-127 to k=128 and skipping 16 lines. It can be seen that the image shown in Fig 4.1e represents the best result. A certain deterioration of image quality is observed in Fig 4.1f as 16 lines are skipped before reconstruction, suggesting that the resulting regular k-space coverage of the image from such a subsampling is not appropriate. This represents a major limitation of the SMASH and SENSE techniques which are based on a regular subsampling of k-space. In the absence of selective excitation, these simulations show that an optimal combination of k-space lines needs to be found in order to achieve the optimal result.

2. Ideal Hadamard Selective excitation:

The previous simulation was repeated by incorporating RF selective excitation profiles. A hadamard-like RF selective excitation profile in the phase encoded direction, $S_e(x, y)$ was used, as shown in Fig 4.2a. A projection of $S_e(x, y)$ onto the phase encoded direction is shown in Fig 4.2i. Figure 4.2e shows the sensitivity profile in one of the coils, Fig 4.2b shows the sought image, Fig 4.2c shows the simulation of the image as it would be received in the coil without the application of the selective

excitation, and Fig 4.2d shows the simulation of the image as it would be received in the coil with the application of the selective excitation. Below each image shown in Figs 4.2b-d, we show the magnitude of its two-dimensional Fourier Transform, equivalent to its k-space profile. It can be seen that the k-space profile shown in Fig 4.2h has the largest spread, suggesting a large mixing between high and low frequency information in the phase encoding direction. This results in a good conditioning of the reconstruction matrix and a preservation of image resolution as shown in Fig 4.3. Sixteen shifted versions in the phase encoding direction of the profile shown in Fig 4.2a were multiplied, pixel by pixel, by sixteen rotated sensitivity profiles (Fig 4.2b), and used to reconstruct the image from only 16 lines of k-space as described in the previous section. These reconstructions are shown respectively in Figs 4.3a-c. Below each image, we show the respective lines of k-space that were used to reconstruct it. These results show that we get perfect reconstructions, regardless of the k-space lines chosen, due to the efficient k-space blurring caused by the selective excitation. Hence, in order to maximize the SNR, we expect that it would be optimal to sample the lower part of k-space as shown in Fig 4.3d.

3. Smooth selective excitation:

A second simulation was performed to show the effect of smooth selective excitation profiles on the reconstruction. A selective excitation profile containing 5 spatial frequencies in the phase encoded direction was synthesized, and is shown in Fig 4.4a. A projection of this profile onto the phase encoded direction is shown in Fig 4.4i and the k-space magnitude of the image shown in Fig 4.4a is shown in Fig 4.4e. The same sensitivity profile shown in Fig 4.3e was used. Figs 4.4b- 4.4d show the SPACE RIP reconstruction using the k-space lines shown in Figs 4.4f- 4.4h respectively. It can be seen that the resolution of the images shown in Figs 4.4c and 4.4d is superior to that of the image shown in Fig 4.4b, confirming our expectations. No difference

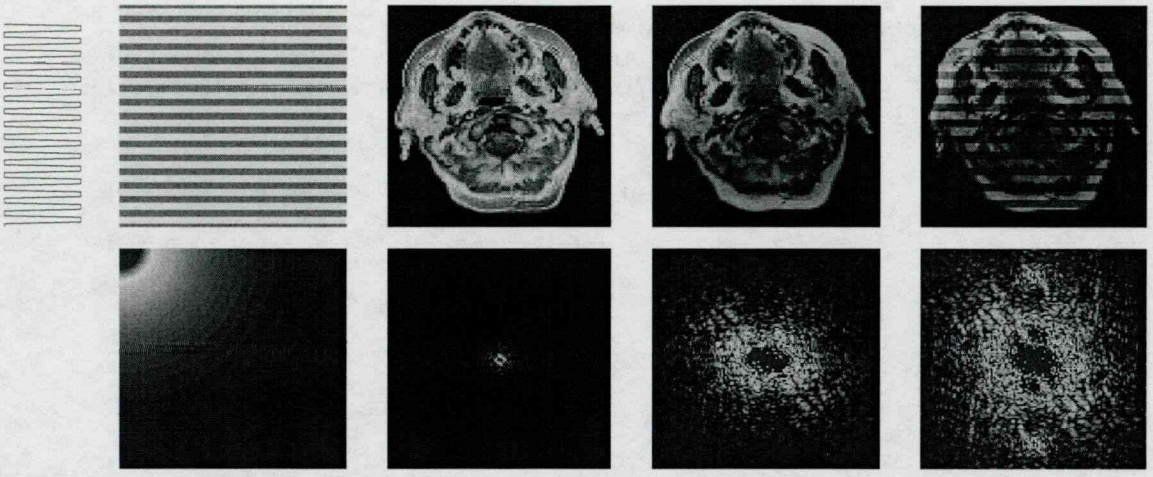

Figure 4.2: Hadamard shaped selective excitation profiles: Fig 4.2a shows a Hadamard excitation profile, Fig 4.2b shows the image to be reconstructed, Fig 4.2e shows a simulated sensitivity profile having a $\frac{1}{r^2}$ falloff, Fig 4.2c shows a simulation of the image weighted by the sensitivity profile shown in Fig 4.2e. Fig 4.2d shows the image weighted by both the sensitivity profile and the selective excitation profile. Below each of Figs 4.2b-d, we show the amplitude of their k-space profile in Figs 4.2f-h respectively.

can be seen between the images shown in Fig 4.4c and Fig 4.4d suggesting that both samplings fully cover the k-space of the image.

4.4 Discussion

Parallel imaging techniques suffer from a number of problems that arise due to the ill-conditioning of the reconstruction process. This is due to the fact that the sensitivity profiles of RF coils are smooth in nature, causing only a slight mixing in the spatial frequencies of the image. Sharp edged sensitivity profiles, if they existed, would allow for a more radical mixing of the spatial frequencies, resulting in better conditioned reconstructions.

The effect of having sharp sensitivity profiles can be mimicked by the use of

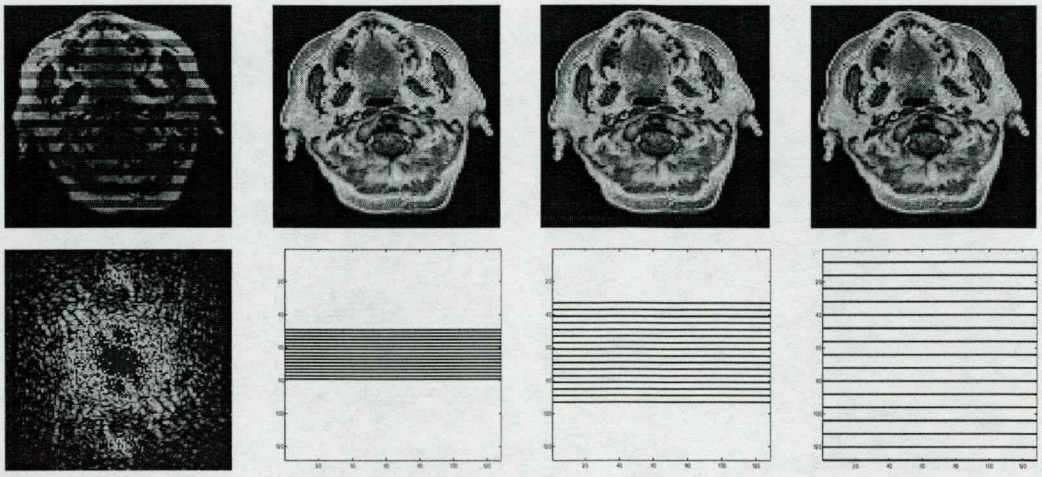

Figure 4.3: Reconstructions after hadamard shaped selective excitation: Figs 4.3a and 4.3e are reproductions of Figs 4.2d and 4.2h. Figs 4.4b- 4.4d show the reconstruction from using 16 k-space lines acquired by skipping respectively from left to right, 1,8 and 16 lines of k-space. Below each image, we show the lines used to reconstruct it.

2D selective excitation RF pulses. These pulses can be designed to excite any 2D structure and when combined with the coil sensitivity profiles can clearly contribute to a high mixing of spatial frequency energy. This can lead to a good conditioning of the image reconstruction matrix, resulting in a preservation of image resolution and SNR in accelerated images. In this chapter, we have combined 2D RF excitation methods with the SPACE RIP technique and shown how these pulses can be designed for maximum efficiency. Our results show that it is feasible to perform real-time accelerated multi-shot gradient recalled echo imaging, with the same quality as non accelerated imaging.

Designing optimal 2D RF excitation pulses requires trading off pulse length versus profile definition. The higher the definition, the longer the RF pulse is, and the slower the sequence becomes. Using 2D selective excitation pulses is particularly advantageous in a multi-shot multi-echo gradient echo sequence as shown in fig 4.5, whereby speed is achieved without a penalty.

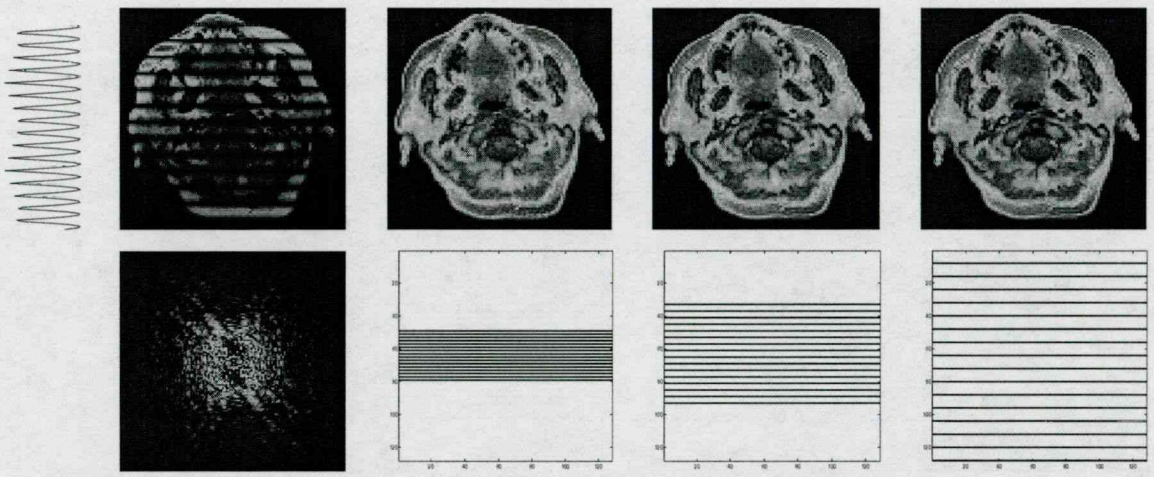

Figure 4.4: Reconstructions after smooth shaped selective excitation: Fig 4.4i shows the projection of a smooth excitation profile along the phase encoded direction. Fig 4.4a shows the image weighted by both the selective excitation profile and by the sensitivity profile shown in Fig 4.2e. Fig 4.4e shows the amplitude of the k-space profile of Fig 4.2a. Figs 4.4b- 4.4d show the reconstruction from using 16 k-space lines acquired by skipping respectively from left to right, 1,8 and 16 lines of k-space. Below each image, we show the lines used to reconstruct it.

Significant reduction of imaging speed can be achieved using this technique. In this chapter, we show the results of a 4-fold speed increase, however, this result can be enhanced depending on the number of coils that are placed into the receiver array. Since there is a tradeoff between coil size and penetration, an optimal number of coils can be computed to yield the best results.

A current practical limitation of this technique is the need for a large number of receivers. Most commercial scanners are limited to four receivers, and the high cost of adding one receiver makes having as much as sixteen of them practically prohibitive. This problem could be solved by the use of channel multiplexers whereby multiple coil outputs could be multiplexed and fed into a single receiver, and later demultiplexed to get the ouput of each one of them. Our technique is based on the use of coil

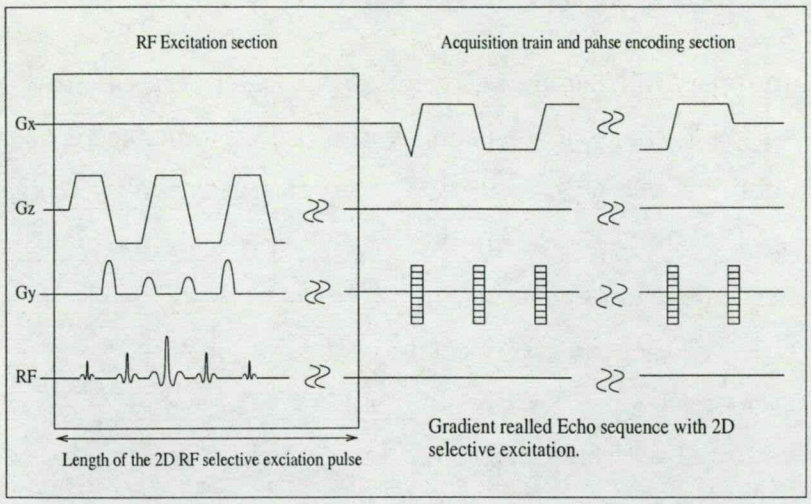

Figure 4.5: left: Selective excitation Gradient echo Pulse sequence.

sensitivity profiles to encode spatial dimensions, therefore, a good estimation of these profiles is crucial to ensure good results. In this chapter, we applied our technique by considering that the sensitivity profiles are independent of the coil loading, allowing us to extrapolate the results of the sensitivity profiles computed from a water phantom and use them to encode other images. In reality however, loading affects the sensitivity profiles of the coil elements, and a dynamic method of profile computation needs to be designed in order to account for the different objects imaged.

The limitations mentioned appear surmountable, as such the technique has great potential to overcome the problem of long acquistion times in MRI. The parallel reconstruction algorithm should allow for real-time acquistion as well as reconstruction of MR data, and may be very well suited for applications such as cardiac imaging and functional imaging as well as interventional imaging [46].

4.5 Conclusion and Future direction:

This thesis reported on a novel parallel imaging technique in MRI termed SPACE RIP. It allows for the speedup of image acquisition by the use of multiple receiver coils, and is capable of combining selective excitation strategies with multi-receiver sensitivity profiles, in order to achieve high frame rates. The feasibility of using selective excitation has been shown in this thesis, however, some work needs to be done in order to optimize the design of the RF selective excitation profiles. Short 2D profiles are required for faster results.

The use of this technique can also be extented to 3D imaging. In this case, the size of the reconstruction matrix is augmented exponentially as shown in section 2.3, and would require large computing resources that are on the order of multiple Gigabytes of RAM on each of an array of processors. These resources may become feasible in the near future thereby enabling the acquisition of 3D data sets in real-time. This would represent a sizeable step for applications such as functional imaging of the brain or cardiac imaging, and would contribute to new medical knowledge about the function of these organs.

Parallel imaging requires the use of multiple receiver channels. Current MRI scanners have up to 4 receiver channels. This limits the acceleration factor to 4. In the future, a larger number of channels will be needed to achieve real-time 3D imaging. More work needs to be done to determine the optimal number of channels required to achieve high resolution, high SNR, real-time 3D imaging. In addition, optimal coil arrays should be designed for specific dynamic applications.

Bibliography

[1] Stark D. D. and W.G. bradley, editors. *Magnetic Resonance Imaging.* C. V. Mosby, Saint-Louis, Mo, 1988.

[2] P. Mansfield and I.L. Pykett. Biological and medical imaging by NMR. *J. Magn. Reson.*, 29:355–373, 1978.

[3] D.M. Kean and M.A. Smith, editors. *Magnetic Resonance Imaging: Principles and applications.* William and Wilkins, Baltimore, MD, 1986.

[4] S.W. Young, editor. *Nuclear Mgnetic Resonance Imaging: Basic Principles.* Raven Press, New York, 1984.

[5] S.L. Talagala and I.J. Lowe. Introduction to magnetic resonance imaging. *Concepts in Magnetic Resonance*, 3:145–159, 1991.

[6] P. Sprawls. *Physical Principles of Medical Imaging.* Aspen Publ., Rockville, MD, 1987.

[7] C.J.. Argersinger R.E. Allen Moore G.A. Bottomley, P.A. Hardy. A review of hydrogen nuclear magnetic resonance relaxation in pathology: Are t1 and t2 diagnostic? *Med. Phys.*, 14.

[8] Bloch F. Nuclear induction. *Phys. Rev.*, 70:460–474, 1946.

[9] T.H. Argersinger R.E. Pfeiffer. L.M. Bottomley, P.A. Foster. A review of normal tissue hydrogen nmr relaxation mechanisms from 1-100 mhz: Dependence on tissue type,nmr frequency, temperature, species, excision and age. *Med. Phys.*, 11:425–460, 1984.

[10] T.C. Farrar and E.D. Becker, editors. *Pulse and Fourier Transform NMR.* Academic Press, New-York, 1971.

[11] D. Twieg. The k-trajectory formulation of the NMR imaging process with applications in analysis and synthesis of imaging methods. *Med. Phys.*, 10(5):610–621, 1983.

[12] Rand SD. Yuan C. Shmiedl UP. Weinberger E. Kruek WR. Three dimensional fast spin-echo imaging: Pulse sequence and in vivo image evaluation. *J. Magn Reson. Med.*, 3:894–899., 1993.

[13] G.A. Morris and R. Freeman. Slice selection in Fourier transform nuclear magnetic resonance. *J. Magn. Reson.*, 29:433–462, 1978.

[14] W.A. Edelstein, G.H. Glover, C.J. Hardy, and R.W. Redington. The intrinsic signal-to-noise ratio in NMR imaging. *Magn. Reson. Imag.*, 3:604–618, 1986.

[15] R.F. Wagner and D.G. Brown. Unified SNR analysis of medical imaging systems. *Phys.Med.Biol.*, 30:489–518, 1985.

[16] J.B. Weaver and D.M. Healy. Signal to noise ratios and effective repetition times for wavelet and adapted waveform encoding. Paper submitted to J. Magn. Reson., 1993.

[17] A. Nishimura D.G. Meyer, C.H. Macovski. Square spiral fast imaging. *Soc. Magn. Reson. Med.*, 362, 1989.

[18] L.P. Panych, P.D. Jakab, and F.A. Jolesz. Progress towards real-time adaptive imaging using wavelet transform encoding. In *SMRM Conference Abstracts*, page 4513, 1992.

[19] Ordidge P. Howesman A. Coxon R. Chapman B. Turner R. Stehling M. Mansfield P. Snapshot head imaging at 0.5t using the echo planar techniques. *Magn. Reson. Med.*, 8:110–116, 1988.

[20] D. Turner, R. Le Bihan. Single-shot diffusion imaging at 2.0 tesla. *J. Magn. Reson.*, 86:445–452, 1990.

[21] A. Kumar, D. Welti, and R.R. Ernst. NMR Fourier zeugmatography. *J.Magn.Reson.*, 18:69–83, 1975.

[22] M.S. Cohen and R.M. Weisskoff. Ultra-fast imaging. *Magn. Reson. Imag.*, 9:1–37, 1991.

[23] A.S. Fram E.K. Atlas, S.W. Mark. Aqueductal stenosis:evaluation with gradient-echo mr imaging. *Radiology*, 1988.

[24] J. Hennig, A. Naureth, and H. Friedburg. RARE imaging: a fast imaging method for clinical MR. *Magn. Reson. Med.*, 3:823–833, 1986.

[25] D. Hanicke W. Maerboldt KD. Haase A. Frahm, J. Matthaei. Flash imaging. rapid nmr imaging using low-flip-angle pulses. *J. Magn. Reson.*, 67:258–266, 1986.

[26] Ordidge P. Howesman A. Coxon R. Chapman B. Turner R. Stehling M. Mansfield P. Glover P. Snapshot imaging at 0.5t using the echo planar techniques. *Magn. Reson. Med.*, 10:227, 1989.

[27] vanGelderen P. Moonen C. Duyn J. Fast volume scanning with frequency shifted burst mri. *Magn. Reson. Med.*, 32:429, 1994.

[28] Feinberg DA. Oshio K. Gase(gradient and spin-echo) imaging: A novel fast mri technique. *Magn. Reson. Med.*, 10:344–349, 1991.

[29] M.E. Brummer, W.T. Dixon, B. Gerety, and H. Tuithof. Composite k-space windows (keyhole techniques) to improve temporal resolution in a dynamic series of images following contrast administration. In *SMRM Conference Abstracts*, page 4236, 1992.

[30] J.D. Weissman and A. Stein. *Physical Principles and Instrumentation*, volume 2 of *Magnetic resonance imaging*, chapter 'Thin-slice MRI'. WB Saunders Co., 1988.

[31] Raff U. Hutchinson M. Fast mri data acquisition using multiple detectors. *Magn Reson Med*, 6:87–91, 1988.

[32] Kwiat D. Einav S. Navon G. A decoupled coil detector array for fast image acquisition in magnetic resonance imaging. *Medical Physics*, 18:251–265, 1991.

[33] Ra JB. Rim CY. Fast imaging using subencoding data sets from multiple detectors. *Magn. Reson. Med.*, 30:142–145, 1993.

[34] Sodickson DK. Manning WJ. Simultaneous acquisition of spatial harmonics (smash): fast imaging with radiofrequency coil arrays. *Magn. Reson. Med.*, 38:591–603, 1997.

[35] Markus B. Scheidegger Klaas P. Pruessmann, Markus Weiger and Peter Boesiger. Sense: Sensitivity encoding for fast mri. *Magn. Res. Med.*, 42:952–962, 1999.

[36] Hingham NJ, editor. *Accuracy and stability of numerical algorithms.* SIAM, Philadelphia, 1996.

[37] Narayama PA. Brey WW. Correction for intensity falloff in surface coil magnetic resonance imaging. *Med. Phys.*, 15:241–245, 1987.

[38] Weinberger E. Murakami JW, Hayes CE. Intensity correction of phased array surface coil images. *Magn. Reson. Med.*, 35:585–590, 1996.

[39] Scheidegger MB Boesiger P. Pruessmann KP, Weiger M. Coil sensitivity maps for sensitivity encoding and intensity correction. In *ISMRM 6th annual meeting, Sydney*, page 2087, 1998.

[40] Dixon WT Tuitho HH Engels H Nelson RC Gerety BM Chezmar JL Den Boer JA. Van Vaals JJ, Brummer ME. "keyhole" method for accelerating imaging of contrast agent uptake. *J Magn. Reson. Imag.*, 3:671–675, 1993.

[41] Jakob PM. Griswold MA. Edelman PR. Manning WJ. Sodickson DK. Accelerated cardiac imaging using the smash technique. *Journal of Cardiovascular Magnetic Resonance*, 1, 1999.

[42] Boesiger P. Weiger M, Pruessmann KP. Cardiac real-time imaging using sense. *Magn. Res. Med.*, 43, 2000.

[43] Walid E. Kyriakos Lawrence P. Panych Daniel F. Kacher Carl-Fredrik Westin Sumi M. Bao Robert V. Mulkern and Ferenc A. Jolesz. Sensitivity profiles from an array of coils for encoding and reconstruction in parallel (space rip). *Magn. Reson. Med.*, 44:301–308, 2000.

[44] Kyriakos WE. Panych LP. Kacher DF. Westin C-F. Bao S. Mulkern RV. Jolesz FA. Parallel image resonstruction from multiple receiver arrays for fast mri. In *ISMRM, Colorado*, 2000.

[45] Panych LP. Oshio K. Selection of high definition 2d virtual profiles with multiple rf pulse excitations along interleaved echo-planar k-space trajectories. *Mag Reson Med*, 41, 1999.

[46] F.A. Jolesz. Interventional magnetic resonance imaging, computed tomography and ultrasound. *Academic Radiology*, 2:S124–S125, 1995.